
Exploiting the Tunable Optical Response of Metallic Nanoshells

3

Ovidio Peña-Rodríguez and Umapada Pal

Contents

1	Definition of the Topic	99
2	Overview	100
3	Introduction	100
4	Experimental and Theoretical Methodologies	102
4.1	Synthesis	102
4.2	Theoretical Methods	105
5	Key Research Findings	115
5.1	Optical Properties	115
5.2	Applications	124
6	Conclusions and Future Perspective	140
	References	141

1 Definition of the Topic

Metallic nanoshells, which are plasmonic nanostructures having alternating layers of dielectric and metal, exhibit a notable structural tunability of the plasmon frequencies. This interesting feature has been exploited for a myriad of applications. In this chapter, along with some synthesis approaches, we discuss the origin of the structural tunability and application potentials of these novel nanostructures in fields such as surface-enhanced Raman scattering, medicine, and photonics.

O. Peña-Rodríguez (✉)

Centro de Microanálisis de Materiales (CMAM), Universidad Autónoma de Madrid (UAM), Madrid, Spain

Instituto de Óptica, Consejo Superior de Investigaciones Científicas (IO-CSIC), Madrid, Spain

U. Pal

Instituto de Física, Benemérita Universidad Autónoma de Puebla, Puebla, Puebla, Mexico

2 Overview

Plasmonic nanoparticles have become an emerging field of study in materials science due to their important applications, ranging from biology to optoelectronics. While the research carried out during the past decade have produced plasmonic nanostructures of different materials, different material combinations, and different geometries to manipulate the position and intensity of their surface plasmon resonance (SPR) emission in accordance with their application requirements, there is still a lot to be done to fully exploit the potentiality of these nanostructures. Nanoshells (NSs) are one of the most interesting plasmonic nanostructures. They present a hard-to-match mixture of interesting properties, combining a simple shape with a remarkable tunability of the optical response. So, it is not surprising that an enormous amount of works studying the synthesis, optical properties, and potential applications of these structures have been reported in recent years.

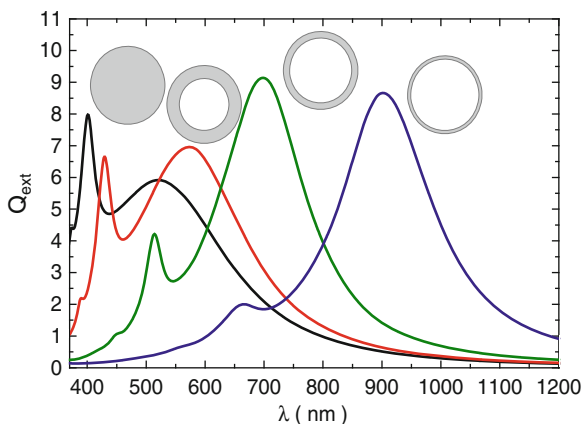
Naturally, different applications have different requirements in terms of size, composition, and morphology of the particles, as well as for the characteristics of the surface plasmon resonance. For example, most biological applications require the maximum of the surface plasmon resonance to be located in the near-infrared region of the spectrum, where biological tissues are transparent. Moreover, *in vivo* applications require that the nanoparticles are chemically inert and small enough to penetrate into the cells, while other applications such as surface-enhanced Raman scattering (SERS) require near electric fields as intense as possible. Therefore, there is no universal recipe for fabricating “good” nanoshells, but, instead, they must be optimized for each individual application. Two factors are of paramount importance for achieving this goal: (1) a detailed knowledge of the factors capable of modifying the optical response of these nanostructures and (2) utilization of synthesis methods suitable for enhancing one feature or the other.

In this chapter, we tried to highlight the progress made on the fabrication of metallic nanoshells, a special kind of plasmonic nanostructure; their application potentials, criteria, and possibilities for tuning their optical responses; advantages over other plasmonic nanostructures; and future application prospects in different fields.

3 Introduction

Metal nanoparticles (NPs) have attracted recently the attention of the scientific community due to their unique electronic and optical properties, which are dominated by the localized surface plasmon resonance (SPR), defined as collective oscillations of the free electrons. For solid nanoparticles, the SPR position barely depends on their geometrical parameters. This behavior is in stark contrast with that of metallic nanoshells [1–3] and their variants [4–6], which exhibit a notable structural tunability of the plasmon frequencies (Fig. 3.1), as has been demonstrated both theoretically [2, 3] and experimentally [7]. This feature makes nanoshells a very interesting kind of particle because, in spite of their simple shape, they can be

Fig. 3.1 Theoretically calculated optical extinction spectra of silver nanoshells ($r_2 = 60$ nm) for some selected core-to-shell ratios (from left to right: 0.0, 0.67, 0.83, and 0.92)



designed to absorb or scatter incident radiation of specific wavelengths, especially in the near-infrared [8]. Before continuing, it is necessary to define what a nanoshell is. It is commonly considered that a nanoshell is a spherical structure composed of a dielectric core and a metallic shell [9]. However, definitions as ample as that of any core-shell structure can also be found in the literature [10]. For the purposes of this chapter, we will define nanoshell as any plasmonic nanostructure having alternating layers of dielectric and metal.

Gold and silver have been traditionally the preferred materials for the synthesis of nanoshells [11–14], and both of them have some advantages and disadvantages. Silver NPs have a more intense SPR, which is of great advantage for surface-enhanced Raman scattering (SERS) and sensing applications. However, gold NPs have better biocompatibility and long-term stability, which make them superior materials for biological applications [1], especially in the form of nanoshells. Moreover, the chemical processes for synthesizing Au nanoshells are well known and easier to perform, allowing a better control over the nanoshell geometry [2].

For various applications like in medical diagnostics [15], immunoassay [16, 17], and studies of living cells and bacteria [18], it is necessary to shift the SPR to the near-infrared region (700–1,300 nm) where the biological tissues are transparent [16]. This can be achieved by increasing the core-to-shell ratio or, in other words, by decreasing the ratio between the thickness of the metallic shell and the total radius [3] of the NPs. Unfortunately, there is a practical limit of attainable red-shift in a conventional nanoshell, which is around 1,200 nm. To overcome this limitation, several attempts have been made to further manipulate the geometry of nanoshell structures. The nanorice [19, 20] (ellipsoidal nanoshells) and nonconcentric [21, 22] and multilayered [6, 23] nanoshells are just a few examples of this strategy, which have increased the limit of allowed red-shifts.

In this work, we intend to review the current state of the art on the fabrication and application of metallic nanoshells. It is somewhat surprising that, despite the intense current pace of research on this area, the summarizing efforts have been rather scarce to date. Probably the first overview of this topic was presented by

Kalele and colleagues in 2006 [10]. Later, in 2009, Erickson and Tunnell [24] published an excellent review chapter analyzing the use of gold nanoshells in biomedical applications. On the other hand, there have been some focused reviews that have compared the performance of nanoshells versus that of different kinds of particles for specific applications, such as the one published by Luk'yanchuk et al. [25] about Fano resonances in plasmonic nanostructures or the book about nanomedicine, edited by Sattler [26]. However, despite these precedents, there has been no effort known to us to present the up-to-date advancements on the fabrication and usage of metallic nanoshells in systematic and collective manner. We believe that this chapter would be of high interest to the scientific community working on design, fabrication, and application of plasmonic nanoshells.

This chapter is divided in four sections, starting with this brief introduction. The second section highlights the progress made on the synthesis of nanoshell structures as well as the theoretical methods used for calculating their optical properties. Precisely these unique optical properties, together with the underlying physics, and the various application prospects of nanoshells are the subjects of the third section. Finally, some concluding remarks have been presented in section four. We hope that this chapter would be useful both for experimental and theoretical researchers as a quick reference, as well as for beginners, to gain hands-on basic knowledge on different aspects of plasmonic nanostructures.

4 Experimental and Theoretical Methodologies

4.1 Synthesis

The first literature report on the synthesis of nanoshells is the one by Zhou et al. [27]. They obtained $\text{Au}_2\text{S}@\text{Au}$ nanoshells via a two-step chemical process. Firstly, they dissolved chloroauric acid ($\text{HAuCl}_4 \cdot 4\text{H}_2\text{O}$) and sodium sulfide ($\text{Na}_2\text{S} \cdot 9\text{H}_2\text{O}$) into super pure water at room temperature to get HAuCl_4 and Na_2S solutions. Then, they mixed controlled amounts of the two solutions together to get unstable gold sulfide (Au_2S) particles. In a second step, they injected a little amount of Na_2S solution into the colloidal Au_2S solution. Finally, the surface of the Au_2S nanoparticles was reduced to obtain the $\text{Au}_2\text{S}@\text{Au}$ nanoshells by injecting chloroauric acid solution. However, they failed to realize the origin of the observed red-shifts of the absorption bands in the composite nanoparticles and assigned them to quantum-size effects. It was not until a few years later when Averitt et al. [9, 28, 29] continued to study this type of nanoshells and determined the classical origin of the observed plasmon shifts.

Subsequently, Oldenburg et al. [2] and Westcott et al. [31, 32] pioneered a new scheme to synthesize nanoshells. In this method, previously manufactured metal nanoparticles were attached to the functionalized surface of a larger dielectric sphere (e.g., SiO_2), and then a complete metallic shell was grown either by further reduction of metal ions [31–34] or through layer-by-layer attachment of prefabricated metal nanoparticles [33, 35] (Fig. 3.2). Usually the preferred

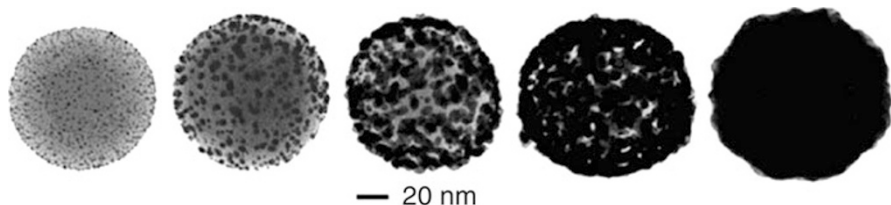


Fig. 3.2 Transmission electron microscopy images of gold nanoshell on a silica dielectric nanoparticle during shell growth [30]

materials for the dielectric core are SiO_2 [31, 32] and polystyrene (PS) [34]. The advantages of the former are its stability and the possibility of using the Stöber method [36] to grow particles of uniform sizes. Use of polystyrene, on the other hand, is advantageous as nanoparticles made of this material can be easily synthesized [37] as monodisperse suspensions, and they can be readily removed later, if desired, obtaining hollow nanoshells. Functionalization of dielectric core can be performed using an ω -terminated trialkoxyorganosilane in the case of SiO_2 [31, 32] or 2-aminoethanethiol hydrochloride in the case of polystyrene spheres [34].

In one of the latter incarnations of this method, Brinson et al. [38] reported a streamlined method for Au layer metallization on prefabricated nanoparticle surfaces using carbon monoxide as the reducing agent. This multistep process was initiated by functionalizing oxide nanoparticles with aminopropyltriethoxy or methoxysilane, followed by the binding of very small (1–2 nm diameter) Au nanoparticles onto the nanoparticle surface to a saturation coverage of nominally 25–30 % [19, 38]. This is subsequently followed by the chemical reduction of $\text{Au}^{3+}_{(\text{aq})} \rightarrow \text{Au}^0_{(\text{s})}$ onto the nanoparticle precursor surface. In the last reduction step, the tiny Au islands grow larger and ultimately merge, resulting in the formation of a continuous, multicrystalline metallic shell layer. They showed that the reduction of Au^{3+} by CO results in the formation of thin, uniform shell layers on these nanoparticles at lower Au^{3+} concentrations, while continuous shell layers were not achievable with existing liquid-phase reduction methods. Since this approach relies only on the introduction of $\text{CO}_{(\text{g})}$ into the solution of prepared precursor nanoparticles and Au^{3+} , the shell layer morphology is not as susceptible to the reaction parameters, like the concentration of reductor or precursor solution, as in other chemical shell growth methods.

Finally, there has also been some interest in making nanoshells by coating SiO_2 and polystyrene spheres using seedless schemes [39–41]. For example, the solvent-assisted route has been used [39] to prepare a complete metal (Ag or Au) shell with controlled thickness on polystyrene colloids. Also, the electroless plating approach, based on electrostatic attraction, has been used to prepare a complete silver shell with controlled thickness on silica colloids. In the first step of the solvent-assisted route (Fig. 3.3a), the PS colloids synthesized by emulsion polymerization [37] are immersed in a mixed solvent of ethanol and acetone containing the metal salt.

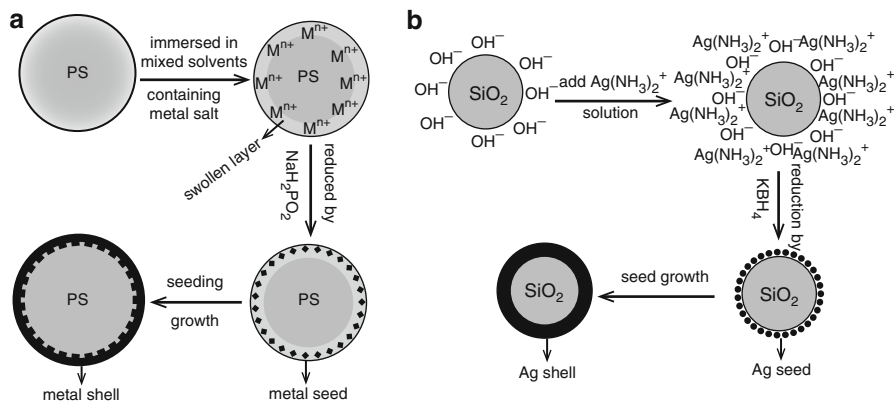


Fig. 3.3 Zhang's procedure for coating (a) polystyrene and (b) silica colloids with metal [39]

During the treatment process, the surface layer of the PS colloids gets swelled by the mixed solvent and permeated by the metal ions. Subsequently, sodium hypophosphite is used to reduce the metal ions in the swollen layer, and the swollen layer of the PS colloids is loaded uniformly with metal nanoparticles. After surface layer seeding, the PS colloids are dispersed in aqueous ethanol containing the metal salt (0.2 M), $C_6H_5O_7Na_3 \cdot 2H_2O$ (0.1 M), and ammonia solution (for Ag coating) or Na_2CO_3 (for Au coating). Then, HCHO (10 %) is added dropwise to grow the metal nanoparticles and increase the density and thickness of the metal shell. By varying the amount of (1) PS colloids after seeding, (2) HCHO, and (3) $C_6H_5O_7Na_3 \cdot 2H_2O$, the thickness and uniformity of the metal shell can be modified effectively.

On the other hand, Zhang's approach for coating silica with silver relies on the surface charge of the as-prepared colloids [36, 42], arising from the negatively charged Si-OH groups (Fig. 3.3b). The $[Ag(NH_3)_2]^+$ ions are absorbed onto the colloids' surface by the negatively charged Si-OH groups through electrostatic attraction. Subsequently, KBH_4 is used to reduce the $[Ag(NH_3)_2]^+$ ions, and the colloids' surface is covered uniformly with silver nanoparticles. The growth of the colloids after surface seeding is similar to that of the PS colloids after surface seeding. The main advantages of the above two coating routes are the following [39]:

1. Metal seeds are synthesized directly on the surface layer of the PS or silica core, avoiding the surface functionalization of the core and additional preparation of metal nanoparticles
2. The thickness and roughness of the metal shell can be effectively controlled through continuous dropwise addition of reductor solution, and the as-prepared core-shell colloids can crystallize into a long-range-ordered structure.
3. The routes are facile and versatile and suitable for the coating of other metals whose cations or complexes can be reduced in solution.

4.2 Theoretical Methods

The methods used for computing the scattering properties of small particles can be roughly divided in two groups: exact and approximated techniques. In general, the exact methods are more accurate than the approximated ones but are much more restricted with respect to the kind of particles they are suited for. All exact techniques for calculating electromagnetic scattering are based on solving the differential Maxwell equations or their integral counterparts in the time or frequency domain. To find an analytical solution, one has to solve the vector wave equations for the time-dependent electric fields outside and inside the particle, using the separation of variables technique. Then, the incident and internal fields are expanded in wave functions which are regular inside the scatterer, whereas the external scattered field is expanded in wave functions that behave as outgoing waves at infinity. Finally, using the requirement of continuity of the tangential component of the electric and magnetic fields at the particle boundary, the unknown coefficients in the internal and scattered field expansions can be determined from the known expansion coefficients of the incident field [43].

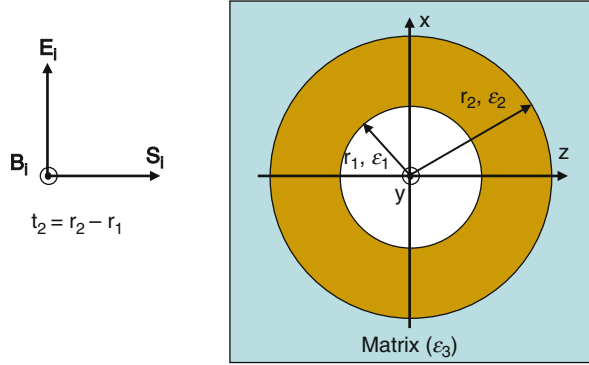
Unfortunately, the separation of variables technique generates only manageable solutions for a few simple cases. The first of such exact solutions was developed by Mie [44] for spherical particles. This model was later extended, first for the coated sphere [45] and then for the multilayered sphere [46–49]. Similar solutions have been found for homogeneous infinite circular cylinders [50], infinite elliptical cylinders [51], and homogeneous and core-mantle spheroids [52]. However, in the case of spherically symmetric particles, like most nanoshell variants, the exact methods can be used to generate accurate results for essentially any size parameter and relative refractive index values. Therefore, in this review we will focus mainly on the exact methods, and the approximate ones will be discussed only briefly, to show in which cases they can replace or supplement the exact solutions.

4.2.1 Quasi-static Approximation

When a particle's size is much smaller than the incident wavelength, the incident electric field may be regarded as spatially uniform over the extent of the particle; this is referred to as the quasi-static (QS) approximation. Despite its simplicity and lack of rigor, this approach is useful for qualitative understanding of the phenomena related to light scattering by nanoshells as it considerably simplifies the mathematical analysis. In this case, the electrostatic solution can be obtained by solving Laplace's equation of the potential.

The expressions needed to calculate the electric field of a core-shell particle in the quasi-static approach were first developed by Neeves and Birnboim [53]. Averitt et al. [28] subsequently extended the analysis, obtaining explicit formulas for the scattering and the absorption cross sections as well as for the geometric tunability of the surface plasmon resonance. In the core-shell geometry (Fig. 3.4), the first region is the core, characterized by a radius r_1 and dielectric function ϵ_1 . The second region (the shell) has a thickness $t_2 = r_2 - r_1$ and a dielectric function ϵ_2 , and, finally, the surrounding medium has a dielectric function ϵ_3 . In general, there is

Fig. 3.4 Schematic representation of a typical metal nanoshell geometry



no especial requirement for the dielectric functions (i.e., each can be either real or imaginary), but this geometry becomes a metal nanoshell when the core is a dielectric material and ε_2 is the dielectric function of a metal. The general solution for the potential in each region is given by:

$$\Phi_i(r, \theta) = [A_i r + B_i/r^2] \cos \theta \quad (3.1)$$

where A_i and B_i are the constants multiplying the monopole and the dipole terms, respectively. $B_1 = 0$ in the core and the potential $\Phi_3 = -E_0 r \cos \theta$ must be recovered in the surrounding medium, far from the shell, yielding $A_3 = -E_0$. Moreover, there must be continuity of the tangential and normal components of the electric field:

$$\left. \frac{\partial \Phi_i}{\partial \theta} \right|_{r=r_i} = \left. \frac{\partial \Phi_{i+1}}{\partial \theta} \right|_{r=r_i} \quad (3.2)$$

$$\varepsilon_i \left. \frac{\partial \Phi_i}{\partial r} \right|_{r=r_i} = \varepsilon_{i+1} \left. \frac{\partial \Phi_{i+1}}{\partial r} \right|_{r=r_i} \quad (3.3)$$

The application of the boundary conditions to Eq. 3.1, together with the known values of A_3 and B_1 , results in a set of four equations and four unknowns that can be solved to obtain the constants A_1 , A_2 , B_2 , and B_3 , allowing the determination of the potential in the core, shell, and embedding medium. The electric field, in turn, can be obtained for each region using the expression $\mathbf{E}_i = -\nabla\Phi_i(r, \theta)$:

$$\mathbf{E}_1 = \frac{9\varepsilon_2\varepsilon_3}{\varepsilon_2\varepsilon_a - 2\varepsilon_3\varepsilon_b} E_0 (\cos \theta \hat{r} + \sin \theta \hat{\theta}) \quad (3.4)$$

$$\mathbf{E}_2 = \frac{3\varepsilon_3}{\varepsilon_2\varepsilon_a - 2\varepsilon_3\varepsilon_b} E_0 \left\{ \begin{aligned} & [(\varepsilon_1 + 2\varepsilon_2) + 2(\varepsilon_1 - \varepsilon_2)(r_1/r)^3] \cos \theta \hat{r} + \\ & + [(\varepsilon_1 + 2\varepsilon_2) - (\varepsilon_1 - \varepsilon_2)(r_1/r)^3] \sin \theta \hat{\theta} \end{aligned} \right\} \quad (3.5)$$

$$\mathbf{E}_3 = \left\{ 2 \frac{\varepsilon_2 \varepsilon_a - \varepsilon_3 \varepsilon_b}{\varepsilon_2 \varepsilon_a - 2\varepsilon_3 \varepsilon_b} \left(\frac{r_2}{r} \right)^3 + 1 \right\} E_0 \cos \theta \hat{r} + \left\{ \frac{\varepsilon_2 \varepsilon_a - \varepsilon_3 \varepsilon_b}{\varepsilon_2 \varepsilon_a - 2\varepsilon_3 \varepsilon_b} \left(\frac{r_2}{r} \right)^3 - 1 \right\} E_0 \sin \theta \hat{\theta} \quad (3.6)$$

where

$$\varepsilon_a = \varepsilon_1(3 - 2P) + 2\varepsilon_2 P \quad (3.7)$$

$$\varepsilon_b = \varepsilon_1 P + \varepsilon_2(3 - P) \quad (3.8)$$

P is the ratio of the shell volume to the total particle volume. The induced field in the region outside the shell is the same as a dipole with an effective dipole moment of $\mathbf{p} = \varepsilon_3 \alpha \mathbf{E}_{ind}$; then, the polarizability is given as:

$$\alpha = 4\pi \varepsilon_0 r_2^3 \left[\frac{\varepsilon_2 \varepsilon_a - \varepsilon_3 \varepsilon_b}{\varepsilon_2 \varepsilon_a - 2\varepsilon_3 \varepsilon_b} \right] \quad (3.9)$$

where $\varepsilon_0 = 8.85 \times 10^{-12}$ F/m is the permittivity of free space. Finally, the scattering and absorption cross sections can be obtained from the polarizability, by using scattering theory [54]:

$$\sigma_{sca} = \frac{k^4}{6\pi \varepsilon_0^2} |\alpha|^2 = \frac{128 \pi^5}{3 \lambda^4} \varepsilon_3^2 r_2^6 \left| \frac{\varepsilon_2 \varepsilon_a - \varepsilon_3 \varepsilon_b}{\varepsilon_2 \varepsilon_a - 2\varepsilon_3 \varepsilon_b} \right|^2 \quad (3.10)$$

$$\sigma_{abs} = \frac{k}{\varepsilon_0} \text{Im}(\alpha) = \frac{8 \pi^2}{\lambda} \sqrt{\varepsilon_3} r_2^3 \text{Im} \left(\frac{\varepsilon_2 \varepsilon_a - \varepsilon_3 \varepsilon_b}{\varepsilon_2 \varepsilon_a - 2\varepsilon_3 \varepsilon_b} \right) \quad (3.11)$$

4.2.2 Mie Theory

The simplest exact solution is the original Mie formulation [44], which is based on solving Maxwell's equations in spherical polar coordinates for an incident electromagnetic (EM) plane wave impinging on a metallic sphere with a radius r embedded in a medium with a refractive index n_m . Now, let us consider an x-polarized incident electric field, $\mathbf{E}_i = E_0 \exp[ikr \cos(\theta)] \hat{e}_x$, with a time dependence of $\exp(-i\omega t)$. The interaction of this EM wave with small particles produces scattering and absorption of the incident plane wave [54]. The total energy loss of the incident radiation is the sum of the scattered and absorbed energies. These energy losses are expressed in a more convenient form by the cross sections, which are a measure of the probability that an event (scattering, absorption, or extinction) will take place. The total extinction cross section σ_{ext} is given by $\sigma_{ext} = \sigma_{sca} + \sigma_{abs}$, where σ_{sca} and σ_{abs} are the scattering and absorption cross sections, respectively.

In order to express these cross sections, it is convenient to define the size parameter x and the relative refractive index m , as:

$$x = k r = \frac{2\pi n_m r}{\lambda} \quad (3.12)$$

$$m = \frac{n_p}{n_m} \quad (3.13)$$

where r is the radius, λ is the light wavelength in vacuum, and n_p and n_m are the refractive indices of the sphere and the surrounding medium, respectively. Here, k and mk represent the wave number in the dielectric medium and in the metallic particle, respectively. The electromagnetic field is divided into two orthogonal subfields that can be deduced from a scalar potential. The solutions are expressed in terms of infinite series where the coefficient constants are obtained from the appropriate boundary conditions at the surface of the sphere. For this case, the cross sections can be calculated as:

$$\sigma_{ext} = \frac{2\pi}{k^2} \sum_{n=1}^{\infty} (2n+1) \text{Re}\{a_n + b_n\} \quad (3.14)$$

$$\sigma_{sca} = \frac{2\pi}{k^2} \sum_{n=1}^{\infty} (2n+1) (|a_n|^2 + |b_n|^2) \quad (3.15)$$

$$\sigma_{abs} = \sigma_{ext} - \sigma_{dis} \quad (3.16)$$

The corresponding efficiency factors can be calculated for all the cross sections from the relation $Q_i = \sigma_i/A$, where $A = \pi r^2$ is the geometrical cross section of the particle. The scattering coefficients, a_n and b_n , can be calculated by the expressions:

$$a_n = \frac{m\psi_n(mx)\psi'_n(x) - \psi'_n(mx)\psi_n(x)}{m\psi_n(mx)\xi'_n(x) - \psi'_n(mx)\xi_n(x)} \quad (3.17)$$

$$b_n = \frac{\psi_n(mx)\psi'_n(x) - m\psi'_n(mx)\psi_n(x)}{\psi_n(mx)\xi'_n(x) - m\psi'_n(mx)\xi_n(x)} \quad (3.18)$$

where ψ_n and ξ_n are the Riccati-Bessel functions, defined as:

$$\psi_n(z) = z j_n(z), \quad \xi_n(z) = z h_n(z) \quad (3.19)$$

being $j_n(z)$ and $h_n(z)$ the spherical Bessel and Hankel functions [55, 56], respectively. The expressions ψ'_n and ξ'_n indicate differentiation with respect to the argument in parentheses.

This Mie solution for the extinction by a single sphere also applies to any number of spheres provided that they have similar diameters and are randomly distributed with enough separations among them (distances larger than the incident wavelength). Under these circumstances, coherent light is not scattered by the spheres and the total scattered energy is equal to the energy scattered by one sphere multiplied by their total number.

Core-Shell Structures

Mie theory was subsequently extended by Aden and Kerker [45] in order to consider the scattering of light by a sphere with a concentric spherical shell embedded in a medium (core-shell structure with radii r_1 and r_2 for the core and the shell, respectively). They obtained new expressions to calculate the coefficients a_n and b_n (Eqs. 3.14–3.16) are still valid:

$$a_n = \frac{\psi_n(y) [\psi'_n(m_2 y) - A_n \chi'_n(m_2 y)] - \psi'_n(y) [\psi_n(m_2 y) - A_n \chi_n(m_2 y)]}{\zeta_n(y) [\psi'_n(m_2 y) - A_n \chi'_n(m_2 y)] - \zeta'_n(y) [\psi_n(m_2 y) - A_n \chi_n(m_2 y)]} \quad (3.20)$$

$$b_n = \frac{m_2 \psi_n(y) [\psi'_n(m_2 y) - B_n \chi'_n(m_2 y)] - \psi'_n(y) [\psi_n(m_2 y) - B_n \chi_n(m_2 y)]}{m_2 \zeta_n(y) [\psi'_n(m_2 y) - B_n \chi'_n(m_2 y)] - \zeta'_n(y) [\psi_n(m_2 y) - B_n \chi_n(m_2 y)]} \quad (3.21)$$

where

$$A_n = \frac{m_2 \psi_n(m_2 x) \psi'_n(m_1 x) - m_1 \psi'_n(m_2 x) \psi_n(m_1 x)}{m_2 \chi_n(m_2 x) \psi'_n(m_1 x) - m_1 \chi'_n(m_2 x) \psi_n(m_1 x)} \quad (3.22)$$

$$B_n = \frac{m_2 \psi_n(m_1 x) \psi'_n(m_2 x) - m_1 \psi_n(m_2 x) \psi'_n(m_1 x)}{m_2 \chi'_n(m_2 x) \psi_n(m_1 x) - m_1 \psi'_n(m_1 x) \chi_n(m_2 x)} \quad (3.23)$$

$$x = k r_1, \quad y = k r_2 \quad (3.24)$$

Multilayered Spheres

Mie theory can also be extended for the radially inhomogeneous (i.e., multilayered) sphere [46–49]. Similarly to the previous cases, the solution of the scattering by a multilayered sphere consists in expressing the EM fields in each layer l in terms of appropriate sets of spherical wave functions. Each layer is characterized by a size parameter $x_l = 2\pi n_m r_l / \lambda = k r_l$ and a relative refractive index $m_l = n_l / n_m$, $l = 1, 2, \dots, L$, where λ is the wavelength of the incident wave in vacuum, r_l is the outer radius of the l th layer, n_m and n_l are the refractive index of the medium outside the particle and its l th component, respectively, and k is the propagation constant. In the region outside the particle, the relative refractive index is $m_{L+1} = 1$. The space is divided into two regions: the region inside the multilayered sphere and the

surrounding medium outside the particle. The electric and magnetic fields (inside and outside the sphere) are considered as the superposition of sets of spherical wave functions. For example, \mathbf{E}_{in} and \mathbf{E}_{out} can be expressed in terms of complex spherical eigenvectors [43]:

$$\mathbf{E}_{in} = \sum_{n=1}^{\infty} E_n \left[c_n^{(l)} \mathbf{M}_{o1n}^{(1)} - i d_n^{(l)} \mathbf{N}_{e1n}^{(1)} \right] \quad (3.25)$$

$$\mathbf{E}_{out} = \sum_{n=1}^{\infty} E_n \left[i a_n^{(l)} \mathbf{N}_{e1n}^{(3)} - b_n^{(l)} \mathbf{M}_{o1n}^{(3)} \right] \quad (3.26)$$

where $E_n = i^n E_0 (2n+1)/n(n+1)$, and $\mathbf{M}_{o1n}^{(j)}$ and $\mathbf{N}_{e1n}^{(j)}$ ($j = 1, 3$) are the vector harmonic functions with the radial dependence of the first kind of spherical Bessel function for $j = 1$ and the first kind of spherical Hankel function for $j = 3$. The explicit expressions for $\mathbf{M}_{o1n}^{(j)}$ and $\mathbf{N}_{e1n}^{(j)}$ can be found elsewhere, for instance, in ► Chap. 4, “UV-Vis Spectroscopy for Characterization of Metal Nanoparticles Formed from Reduction of Metal Ions During Ultrasonic Irradiation” of reference [54].

In the region outside the sphere, the total external field is the superposition of the incident and scattered fields, $\mathbf{E} = \mathbf{E}_i + \mathbf{E}_s$, which can be expanded as:

$$\mathbf{E}_i = \sum_{n=1}^{\infty} E_n \left[\mathbf{M}_{o1n}^{(1)} - i \mathbf{N}_{e1n}^{(1)} \right] \quad (3.27)$$

$$\mathbf{E}_s = \sum_{n=1}^{\infty} E_n \left[i a_n \mathbf{N}_{e1n}^{(3)} - b_n \mathbf{M}_{o1n}^{(3)} \right] \quad (3.28)$$

where a_n and b_n are the scattering coefficients. It can be deduced [43] that $a_n^{(1)} = b_n^{(1)} = 0$ and $c_n^{(L+1)} = d_n^{(L+1)} = 1$. The expansion coefficients ($a_n^{(l)}$, $b_n^{(l)}$, $c_n^{(l)}$, and $d_n^{(l)}$) and scattering coefficients (a_n and b_n) are obtained by matching the tangential components of EM fields at each interface and after some algebra (for details see reference [43]); the final coefficients in the series can be identified with the scattering coefficients [43]:

$$a_n = a_n^{L+1} = \frac{[H_n^a(m_L x_L)/m_L + n/x_L] \psi_n(x_L) - \psi_{n-1}(x_L)}{[H_n^a(m_L x_L)/m_L + n/x_L] \zeta_n(x_L) - \zeta_{n-1}(x_L)} \quad (3.29)$$

$$b_n = b_n^{L+1} = \frac{[m_L H_n^b(m_L x_L) + n/x_L] \psi_n(x_L) - \psi_{n-1}(x_L)}{[m_L H_n^b(m_L x_L) + n/x_L] \zeta_n(x_L) - \zeta_{n-1}(x_L)} \quad (3.30)$$

where ψ_n and ζ_n are the Riccati-Bessel functions (as defined in reference [57]), and the determinants H_n^a and H_n^b can be calculated by the expressions [43]:

$$H_n^a(m_1 x_1) = D_n^{(1)}(m_1 x_1) \quad (3.31a)$$

$$H_n^a(m_l x_l) = \frac{G_2 D_n^{(1)}(m_l x_l) - Q_n^{(l)} G_1 D_n^{(3)}(m_l x_l)}{G_2 - Q_n^{(l)} G_1}, \quad l = 2, \dots, L \quad (3.31b)$$

$$H_n^a(m_l x_l) = \frac{G_2 D_n^{(1)}(m_l x_l) - Q_n^{(l)} G_1 D_n^{(3)}(m_l x_l)}{G_2 - Q_n^{(l)} G_1}, \quad l = 2, \dots, L \quad (3.32a)$$

$$H_n^b(m_l x_l) = \frac{\tilde{G}_2 D_n^{(1)}(m_l x_l) - Q_n^{(l)} \tilde{G}_1 D_n^{(3)}(m_l x_l)}{\tilde{G}_2 - Q_n^{(l)} \tilde{G}_1}, \quad l = 2, \dots, L \quad (3.32b)$$

and

$$D_n^{(1)}(z) = \psi_n'(z) / \psi_n(z) \quad (3.33)$$

$$D_n^{(3)}(z) = \zeta_n'(z) / \zeta_n(z) \quad (3.34)$$

$$Q_n^{(l)} = \frac{\psi_n(m_l x_{l-1})}{\zeta_n(m_l x_{l-1})} \Big/ \frac{\psi_n(m_l x_l)}{\zeta_n(m_l x_l)} \quad (3.35)$$

$$G_1 = m_l H_n^a(m_{l-1} x_{l-1}) - m_{l-1} D_n^{(1)}(m_l x_{l-1}) \quad (3.36)$$

$$G_2 = m_l H_n^a(m_{l-1} x_{l-1}) - m_{l-1} D_n^{(3)}(m_l x_{l-1}) \quad (3.37)$$

$$\tilde{G}_1 = m_{l-1} H_n^b(m_{l-1} x_{l-1}) - m_l D_n^{(1)}(m_l x_{l-1}) \quad (3.38)$$

$$\tilde{G}_2 = m_{l-1} H_n^b(m_{l-1} x_{l-1}) - m_l D_n^{(3)}(m_l x_{l-1}) \quad (3.39)$$

As before, Eqs. 3.14–3.16 remain valid for the calculation of the cross sections.

4.2.3 Plasmon Hybridization

As has been said earlier, for most nanoshell variants, Mie theory can be used to generate accurate results for essentially any size parameter and relative refractive index values. However, even if one can easily calculate the optical responses of such low-dimensional structures, it is often very difficult to understand the origin of the observed resonances. This problem can be overcome using the theory of plasmon hybridization [6], which is in good agreement with the Mie theory in the dipole limit (i.e., the quasi-static approximation). The theory of plasmon hybridization is an electromagnetic analog of molecular orbital theory, where the characteristics of the SPR can be explained in terms of the interactions between the plasmons of metallic nanostructures of simpler shapes. For example, the SPR of metallic nanoshells (Fig. 3.5) can be viewed as the interaction between the plasmons of a sphere and a cavity. The hybridization of the plasmon of the sphere

Fig. 3.5 Energy-level diagram describing the plasmon hybridization in metal nanoshells, resulting from the interaction between the sphere and cavity plasmons. The two nanoshell plasmons are an antisymmetrically coupled (antibonding) $|\omega_+\rangle$ plasmon mode and a symmetrically coupled (bonding) $|\omega_-\rangle$ plasmon mode

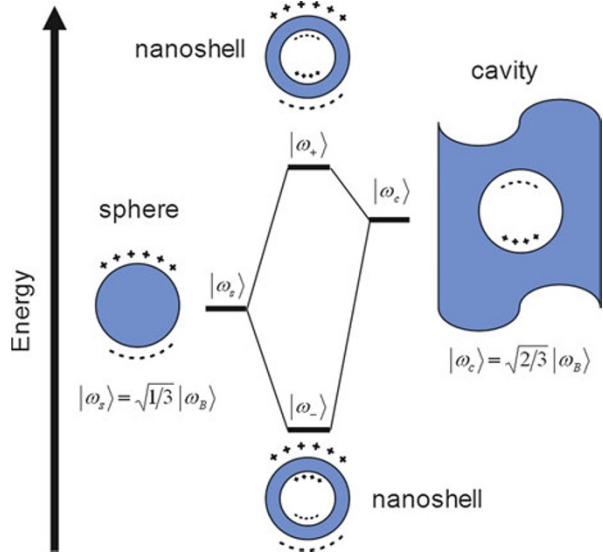
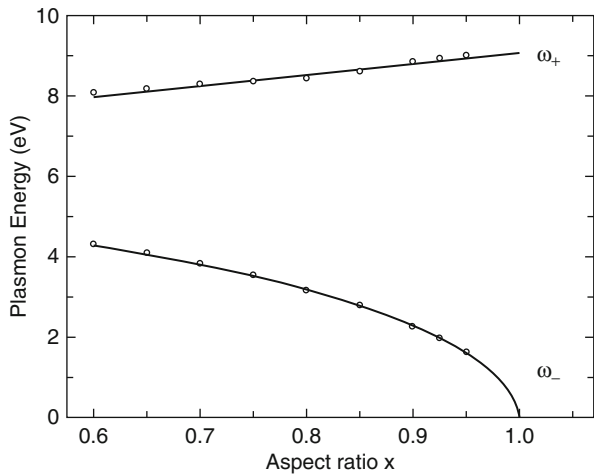


Fig. 3.6 Comparison of calculated symmetric ω_- and antisymmetric ω_+ plasmon resonances (symbols) for gold nanoshells, as a function of their aspect ratio $x = r_1/r_2$ with the result from the semiclassical approximation (Eq. 3.40) (lines) [58]



and the cavity creates two new plasmon oscillation modes (Fig. 3.6), i.e., the higher energy (antibonding) mode $|\omega_+\rangle$ and the lower energy (bonding) mode $|\omega_-\rangle$, corresponding to the antisymmetric and symmetric interactions between the $|\omega_s\rangle$ and $|\omega_c\rangle$ modes, respectively. The frequencies of these modes are [6]:

$$\omega_{l\pm}^2 = \frac{\omega_B^2}{2} \left[1 \pm \frac{1}{2l+1} \sqrt{1 + 4l(l+1) \left(\frac{r_1}{r_2}\right)^{2l+1}} \right] \quad (3.40)$$

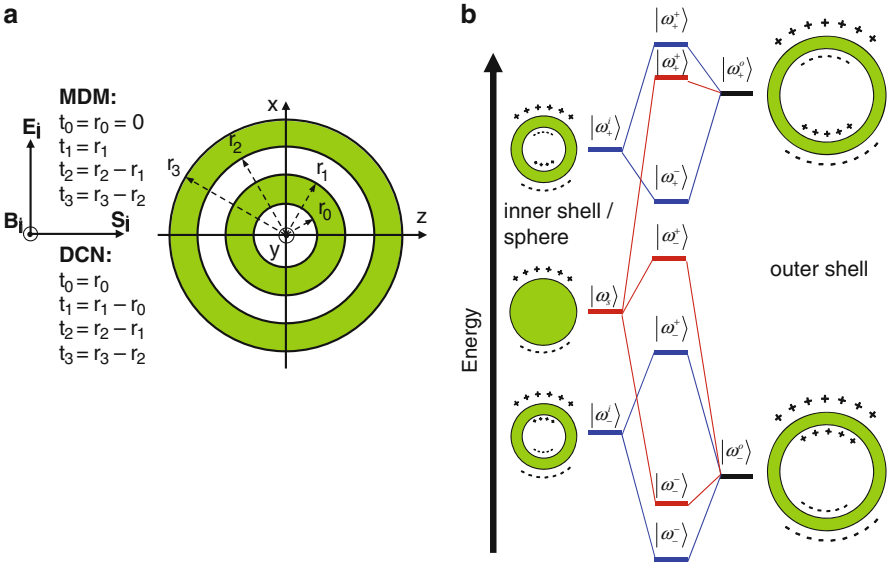


Fig. 3.7 (a) Schematic representation of the MDM and DCN structures (for the MDM $r_0 = t_0 = 0$) and (b) their corresponding energy diagrams, representing plasmon hybridization [59]. Plasmon hybridization for the MDM and DCN structures is represented in red and blue, respectively

being l the plasmon order ($l = 1$ is the dipolar plasmon, $l = 2$ the quadrupolar, and so on), ω_B the bulk plasmon frequency, and r_1 and r_2 the core and shell radii, respectively.

For composite metallic nanostructures of greater geometrical complexity, it is more difficult to obtain explicit expressions for the hybridized modes. However, this method remains as a useful tool to understand qualitatively their plasmon resonance behavior. Two particularly interesting multilayer geometries are metal-dielectric-metal (MDM) [5] and double concentric nanoshells (DCN) [60] structures (Fig. 3.7). The plasmon resonance in a MDM [DCN] structure can be viewed as the interaction between the plasmon responses of the inner sphere [nanoshell] ($|\omega_s^i\rangle$ [$|\omega_-^i\rangle$ and $|\omega_+^i\rangle$]) and the outer ($|\omega_-^o\rangle$ and $|\omega_+^o\rangle$) nanoshell. Three hybridized modes are obtained for the MDM; the energy mode $|\omega_-^s\rangle$ corresponds to the antisymmetric coupling between the symmetric plasmon resonance modes of the outer ($|\omega_-^o\rangle$) nanoshell and the sphere plasmon. The coupling between the higher-energy antibonding mode of the outer nanoshell and the nanosphere plasmon modes is very weak, and only one hybridized mode is produced in this case ($|\omega_+^s\rangle$). In contrast, four hybridized modes are produced in the DCN structure because its inner nanoshell has two energy modes. The energy mode $|\omega_-^s\rangle$ ($|\omega_-^s\rangle$) corresponds to the antisymmetric (symmetric) coupling between the symmetric plasmon resonance modes of the inner ($|\omega_-^i\rangle$) and outer ($|\omega_-^o\rangle$) nanoshells. On the other hand, the energy mode $|\omega_+^s\rangle$ ($|\omega_+^s\rangle$) corresponds to the symmetric (antisymmetric) coupling between the antisymmetric plasmon resonance modes of the inner ($|\omega_+^i\rangle$) and outer

($|\omega_+^o\rangle$) nanoshells (Fig. 3.7). Although, in principle, there exists also a coupling between the antisymmetric and symmetric plasmons of the separate nanoshells, it has only a small influence on the hybridized modes, due to the large energy separation between those two modes [6].

4.2.4 Other Methods

Generally, the above mentioned methods are sufficient to study the optical properties of most of the classical nanoshells. However, there are some interesting cases such as nonconcentric [61], incomplete [41, 62–64], or ellipsoidal [19, 20] nanoshells that require the use of more elaborated techniques. These approximate techniques allow the study of virtually any shape. However, they have the disadvantage that their computational cost is much higher than that of the exact methods. Here, we will briefly discuss two of the methods that are frequently used for this task: the finite-difference in the time-domain (FDTD) method and the discrete dipole approximation (DDA).

The FDTD method, introduced in 1966 by Yee [65], is an electromagnetic modeling technique frequently used for the computation of light scattering by nonspherical or inhomogeneous particles. In this approach, the computational space and time are divided into a grid of discrete points, and the derivatives of the Maxwell equations are approximated by finite differences. The entire volume, containing the scatterer, is discretized into a cubical grid known as the Yee lattice; the basic element of this lattice is the Yee cell [65]. A finite differences method is then applied to evaluate the space and time derivatives of the field. This procedure is repeated iteratively for increasing values of time until a steady state solution is obtained. Absorbing boundary conditions are used to truncate the computational domain; this requires a layer of grid cells all around the computational domain. The absorbing boundary conditions ensure that the wave is not reflected at the open boundary of the discretized volume. Finally, a near- to far-field transformation is used to compute the scattered far-field from the near-field values of the computational domain.

The DDA method was originally developed by Purcell and Pennypacker [66] to model the interaction of light with dust particles in space. The main idea behind the DDA is to simulate the optical response to an electromagnetic field by approximating the particle with a finite number of polarizable entities on a cubic grid. Each dipole cell is assigned a complex polarizability, which can be computed from the complex refractive index of the bulk material and the number of dipoles in a unit volume. For a finite array of point dipoles, the scattering problem may be solved exactly, so the only approximation made in the DDA is the replacement of the continuum target by an array of N -point dipoles. The replacement requires specification of both the geometry (location of the dipoles) and the dipole polarizabilities. This method was further refined by Draine et al. [67, 68], who applied the Fast Fourier Transform and conjugate gradient method to calculate the convolution problem arising in the DDA methodology which allowed the calculation of scattering by larger targets.

5 Key Research Findings

5.1 Optical Properties

The main feature that differentiates nanoshells from solid particles is that, while the surface plasmon resonance of the former can be adjusted by varying the geometric parameters [2], that of the latter is essentially fixed. For example, coating of metallic shells on silica allows one to tune their absorption band from visible to infrared region. Moreover, by changing the shell thickness, one can tune the SPR band position in the desired wavelength range. Metal nanoshells having plasmon resonance in the infrared region are well suited for biological applications, as this range of the electromagnetic spectrum is transparent for biological tissues [69]. Thin metallic layers lead to larger SPR red-shifts, whereas thick layers have the opposite effect [58]. Small variations of shell thickness can displace the SPR in a wide spectral region, which can be optically monitored following the position of their SPR peaks. In this subsection, we will discuss the origin of this interesting feature and analyze the main factors affecting the optical properties of metallic nanoshells.

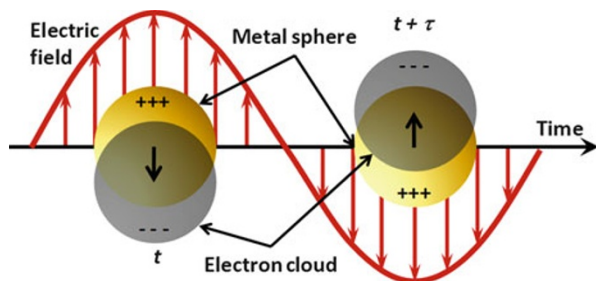
5.1.1 Surface Plasmon Resonance (SPR)

Physical properties of nanoparticles (NP) are intermediate between those of atoms and solids. The range of variation is large because these properties evolve in a nonlinear fashion with increasing number of atoms from a single atom to a dimer, a trimer, and so on, up to the physical properties of a bulk solid. Specifically, the optical properties strongly depend on the size and geometry of the NP [70]. In this respect, surface plasmon resonances (SPRs), coming from the resonant interaction between the collective oscillations of electrons in the conduction band and the incident radiation, play an important role in the optical properties of metals. They give rise to a strong absorption band in the visible range of the electromagnetic spectrum [54, 71]. When the electric field interacts with a metal, its electrons oscillate back and forth at the fluctuation frequency of the incident wave (see Fig. 3.8). The light is reflected because the electrons in the metal act as a shield against the incident electric field. However, there is a frequency fluctuation limit for which electrons can respond; i.e., if the fluctuations are too fast, the electrons can no longer respond. This limit, in which electron-plasma interactions give rise to the absorption of the photon energy, is called the plasmon frequency (ω_p). Light with frequency above the plasma frequency is transmitted. The plasmon frequency is responsible, among other things, for the color of bulk metals like gold and copper. In the free electron model, the plasmon energy can be estimated as:

$$\omega_p = \sqrt{\frac{n e^2}{\epsilon_0 m^*}} \quad (3.41)$$

where n is the density of free electrons, e is the electronic charge, ϵ_0 is the permittivity of free space, and m^* is the effective mass of the electrons.

Fig. 3.8 Schematic representation of the surface plasmon resonance excited by light with a frequency $1/\tau$



Plasmon energy for bulk gold (9.2 eV [72]) and silver (9.0 eV [73]) lies in the UV range; however, for nanoparticles, the plasmon energy is smaller and lies in the UV-visible spectral range. As the electromagnetic wave striking the metal surface has small penetration depth, its interaction with the electrons of the metal surface becomes significant, and the collective oscillations of these surface electrons are known as surface plasmons. The extinction efficiency (Q_{ext}) for spherical metallic particles can be approximated by:

$$Q_{ext} = \frac{24\pi R \varepsilon_m^{3/2}}{\lambda} \frac{\varepsilon'}{(\varepsilon' + 2\varepsilon_m)^2 + (\varepsilon'')^2} \quad (3.42)$$

where R is the radius of the particle, λ the wavelength of the incident electromagnetic radiation, ε' and ε'' are the real and imaginary parts of the dielectric constant of the particles (i.e., $\varepsilon_p = \varepsilon' + i\varepsilon''$), respectively, and ε_m is the dielectric constant of the embedding medium. Then, the extinction would be maximum when $\varepsilon_p + 2\varepsilon_m = 0$, which gives rise to a surface plasmon resonance (SPR) band. The position of the SPR band is dependent on the size and shape of the particle and dielectric constant of the medium in which the particles are dispersed [70].

5.1.2 Dielectric Functions

The optical properties of materials can be described by the complex refractive index ($\tilde{n} = n + ik$) or, alternatively, using the dielectric function ($\varepsilon = \varepsilon' + i\varepsilon''$). Both quantities are equivalent and are related by the expression: $\varepsilon = \tilde{n}^2$. They can be taken either from experimental results or from theoretical models. The most commonly used experimental data for the dielectric function of the noble metals comes from the measurements performed by Johnson and Christy in 1972 [74]. The experimental data published by Palik [75] has been frequently used as well. Unfortunately, the experimental data are not always suitable, as they might have gaps in certain regions of the spectrum or cannot be used with certain calculation algorithms (e.g., FDTD [76]). For this reason, in some cases, analytical expressions for $\varepsilon(\omega)$ are necessary. The more common approach to obtain such expressions consists in adding a certain number of Lorentzian terms to the free-electron (Drude) equation, in order to reproduce the interband transitions; this method is called the extended Drude model (EDM):

$$\varepsilon(\omega) = \varepsilon_\infty - \frac{\omega_p^2}{\omega^2 + j\omega\Gamma} + \sum_{i=0}^n L_i(\omega) \quad (3.43)$$

where the first two terms are the contributions of the standard Drude model, with a high-frequency limit dielectric constant ε_∞ , a plasma frequency ω_p , and a (bulk) damping term Γ , while the $L_i(\omega)$ terms are the frequency-dependent Drude-Lorentz oscillators. Examples of the use of this approach are frequent in the literature. For instance, Vial et al. [77] provided an analytical fit to the gold data using only one Lorentzian term, while See et al. [78], Lee and Gray [79], and Moskovits et al. [80] have represented the dielectric function of silver using two, three, and four Lorentzian terms, respectively. Likewise, Hao and Nordlander [76] and Rakic et al. [81] fitted the dielectric functions of both Au and Ag using four and six Lorentzian terms, respectively.

More recently, Etchegoin et al. [82] have proposed a different approach: replacing the Lorentzian terms with a family of analytical models, called critical points (CPs), which have long been used for the analysis of interband transitions in semiconductors [83]. The advantage of using the CPs is that, unlike simple Lorentz oscillators, they allow for an easy adjustment of asymmetric line shapes [82, 84]. In this approach, the frequency-dependent dielectric function in the near-UV/visible region can be represented by the formula:

$$\varepsilon(\omega) = \varepsilon_\infty - \frac{\omega_p^2}{\omega^2 + j\omega\Gamma} + \sum_{i=0}^n G_i(\omega) \quad (3.44)$$

where $G_i(\omega)$ terms are the critical point oscillators, which can be described by the expression [85]:

$$G_i(\omega) = C_i [e^{j\varphi_i}(\omega_i - \omega - j\Gamma_i)^{\mu_i} + e^{-j\varphi_i}(\omega_i + \omega + j\Gamma_i)^{\mu_i}] \quad (3.45)$$

here, C_i is the amplitude, φ_i the phase, ω_i the energy of the gap, Γ_i the broadening, and μ_i the order of the pole. The form of the dielectric function described by Eqs. 3.45 and 3.46 conforms to the requirements of the Kramers-Kronig relations [80], as long as $\mu_i < 0$ [85].

Size Corrections

Although the optical properties of nanostructured materials differ from those of their bulk counterparts, it is possible to use the dielectric functions determined for bulk metals, $\varepsilon_{bulk}(\omega)$, if the appropriate size corrections are applied. These dielectric functions have contributions from interband and intraband transitions:

$$\varepsilon_{bulk}(\omega) = \varepsilon_{inter}(\omega) + \varepsilon_{intra}(\omega) \quad (3.46)$$

In metals, the electrons at the Fermi level can be excited by photons of very small energies, and therefore, they are considered “free” electrons. The contributions from free electrons to $\varepsilon_{exp}(\omega)$ can be described by the Drude model [54]:

$$\varepsilon_{\text{int } ra}(\omega) = 1 - \frac{\omega_p^2}{\omega^2 + i\omega\Gamma} \quad (3.47)$$

where ω_p is the plasma frequency and Γ the damping constant arising from the dispersion of the electrons. Γ is related with the mean free path of electrons (λ_e) by the expression $\Gamma = v_F/\lambda_e$, being v_F the Fermi velocity.

Now, we must consider that these free electrons can also be dispersed by the NP surface, as their mean free path is comparable or larger than the dimension of the particle. Therefore, it is necessary to modify the damping term to take into account the surface scattering of the “free” electrons:

$$\Gamma = \Gamma_{\text{bulk}} + \Gamma_R = \frac{v_F}{\lambda_e} + \frac{v_F}{R} \quad (3.48)$$

where Γ_R is the damping constant arising from the surface scattering associated with a particle of radius R .

From the Eq. 3.46, we obtain the input of the bound charges by subtracting the free electron contribution from the bulk dielectric function. The free electron contributions are calculated using the Drude model (Eq. 3.47) and ω_p is calculated using Eq. 3.41. Now, we include the surface damping contribution by adding the extra damping term v_F/R to the Drude model and obtain the size-dependent dielectric function, which includes the contributions of the free electrons, surface damping, and interband transitions, as:

$$\begin{aligned} \varepsilon(\omega, R) &= \varepsilon_{\text{inter}}(\omega) + \varepsilon_{\text{intra}}^{\text{NP}}(\omega, R) = \varepsilon_{\text{bulk}}(\omega) - \varepsilon_{\text{intra}}(\omega) + \varepsilon_{\text{intra}}^{\text{NP}}(\omega, R) \\ &= \varepsilon_{\text{bulk}}(\omega) + \frac{\omega_p^2}{\omega^2 + i\omega\Gamma_{\text{bulk}}} - \frac{\omega_p^2}{\omega^2 + i\omega\left(\Gamma_{\text{bulk}} + \frac{v_F}{R}\right)} \end{aligned} \quad (3.49)$$

Up to now we have considered a sphere of radius R , for which the surface damping is given by v_F/R . This correction can easily be extended for a nanoshell if instead of the radius we consider its thickness (t): v_F/t . In both cases, the smaller the particle size (its radius or thickness), the more important is the surface dispersion effect. It has been demonstrated that the surface dispersion effects do not change the location of the surface modes, but they affect the coupling of such modes with the applied field, making the resonance peaks wider and less intense [86].

Just to illustrate the importance of the above-described correction in the values of the dielectric functions, we can analyze how the damping constant changes due to the surface dispersion effect for the case of Cu, which has a Fermi velocity of 1.57×10^6 m/s and a mean free path of electrons of 3.9×10^{-8} m [87], and hence $\Gamma_{\text{bulk}}^{\text{Cu}}$ has a value of $\sim 4.03 \times 10^{13}$ s⁻¹. For a Cu nanoshell with a thickness of 5 nm, $\Gamma_{t=5\text{nm}}^{\text{Cu}}$ is $\sim 3.54 \times 10^{14}$ s⁻¹, one order of magnitude higher than the damping constant for the bulk material.

5.1.3 Tuning the SPR Plasmon Position

Perhaps the single most important characteristic of gold nanoshells is the tunability of their surface plasmon resonance. Among the three geometrical parameters of the nanoshells, the shell thickness (t_2), the radii of the inner core (r_1), and the outer shell (r_2), only two are independent, as: $r_2 = r_1 + t_2$. Consequently, the position of the SPR peak and the relative contributions of absorption and scattering to total extinction can be adjusted simply by varying two of these parameters (Fig. 3.10). Moreover, it has been shown that the position of the SPR depends only on the core-to-shell ratio (r_1/r_2) or, equivalently, on the shell thickness-to-total radius ratio (t_2/r_2) [28]. For greater core-to-shell ratios (thinner shells), the peak becomes shifted to longer wavelengths. This resonance condition can be obtained from Eq. 3.9, when the real part of the denominator becomes zero; i.e., $\text{Re}(\varepsilon_2 \varepsilon_a + 2\varepsilon_3 \varepsilon_b) = 0$. Now, if we assume that the core and the embedding medium are dielectrics (i.e., $\text{Im}(\varepsilon_i) = 0$; $i = 1, 3$), then the expression for the resonance condition as a function of wavelength can be described as [28]:

$$\frac{r_1}{r_2} = \left[1 + \frac{3}{2} \frac{\varepsilon_2'(\lambda)(\varepsilon_1 + 2\varepsilon_3)}{[\varepsilon_2'(\lambda)]^2 - \varepsilon_2'(\lambda)(\varepsilon_1 + 2\varepsilon_3) + \{\varepsilon_1 \varepsilon_3 - [\varepsilon_2''(\lambda)]^2\}} \right]^{1/3} \quad (3.50)$$

where ε_2' and ε_2'' are the real and imaginary part of the shell's dielectric function, respectively.

Equation 3.50 gives the ratio of the core radius to the total radius needed to obtain a resonant condition at a particular wavelength. As can be seen in Fig. 3.9, there is always (within a certain range) a core-to-shell ratio capable of placing the maximum of the SPR in any desired wavelength. For example, the position of the resonant extinction peak of gold nanoshells can be selectively tuned from 590–600 nm to around 1,000 nm (Fig. 3.10a). This wavelength range is especially significant because it includes the “NIR tissue window” from 700 to 1,300 nm (Fig. 3.11) [88], where human tissues are mostly transparent to the incident radiation. In the NIR region, effective penetration depths vary from a few millimeters to several centimeters, depending on tissue type [89, 90]. Precisely this possibility of shifting the nanoshells' SPR to the NIR region is fundamental for their usage on in vivo applications.

Unfortunately, some problems arise when large red-shifts of the SPR are needed; as we have seen, this can only be achieved by increasing the r_1/r_2 ratio. This implies that we have to either reduce the thickness of the metal layer or to increase the particle size. Decreasing the thickness of the metal layer has the disadvantage that the intensity of the near-field is reduced, while increasing the particle size affects the Q_{abs}/Q_{sca} ratio. Both of these effects are unfavorable for some applications, such as surface-enhanced spectroscopy and thermal therapy of tumors [91]. Moreover, after a certain point, the SPR intensity is considerably reduced (Fig. 3.10b), eliminating most of the advantages obtained by the use of nanoshells. Finally,

Fig. 3.9 Core-to-shell ratios necessary to shift the SPR peak to the desired wavelength position, calculated for the three noble metals using Eq. 3.50

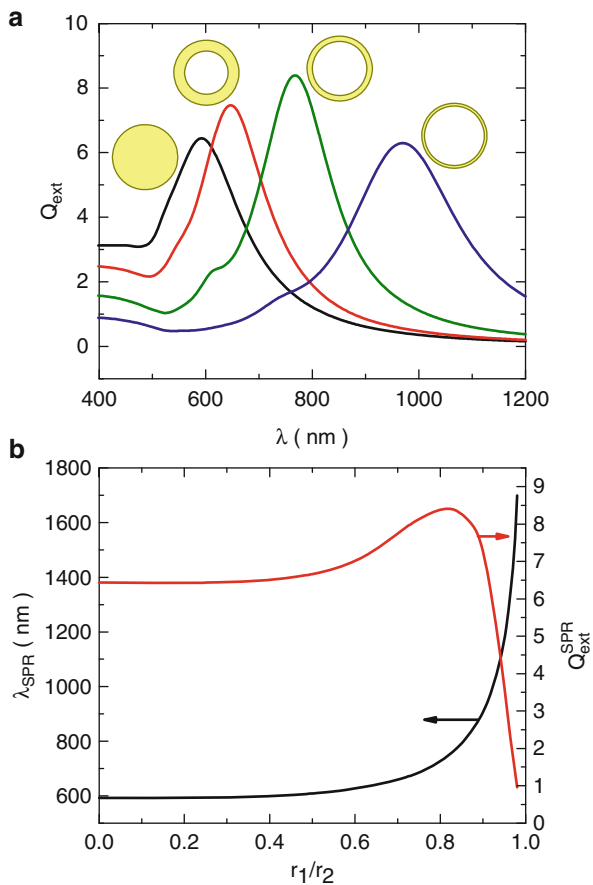
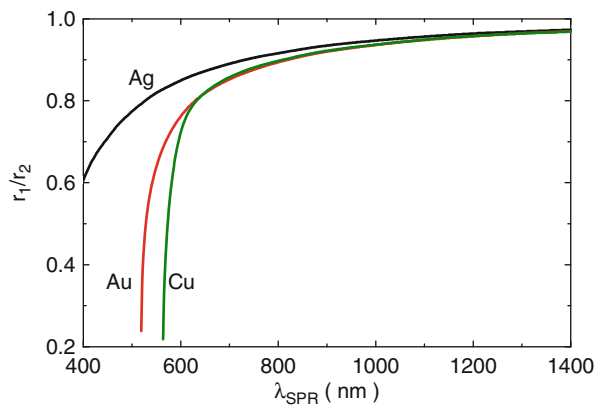


Fig. 3.10 (a) Theoretically calculated optical extinction spectra of gold nanoshells ($r_2 = 60$ nm) for some selected core-to-shell ratios (from left to right: 0.0, 0.67, 0.83, and 0.92). (b) Variation of calculated optical resonance wavelength (black line) and intensity (red line) with core-to-shell ratio for the same metal nanoshells

Fig. 3.11 Optical window in tissue due to reduced absorption of red and near-infrared wavelengths (700–1,300 nm) by tissue chromophores [88]

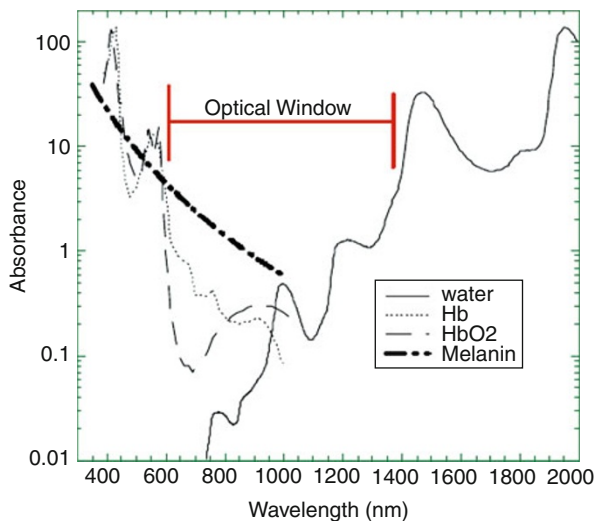
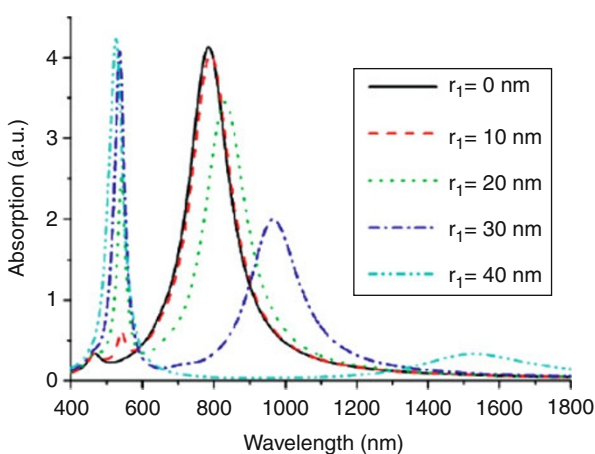


Fig. 3.12 Absorption spectra of MDM nanoshells suspended in free space with $r_1 = 0$ nm (solid line), 10 nm (dashed line), 20 nm (dotted line), 30 nm (dash-dot line), and 40 nm (dash-dot-dot line) [5]



smaller nanoparticles are preferred in certain cases. For instance, use of nanoshells as contrasting agents in biomedicine requires particles of a few tens of nanometer diameters to facilitate their penetration into the biological tissues.

A simple, yet effective, alternative to single nanoshells can be the structures with additional metallic layers, which can produce additional red-shifts through plasmon hybridization while maintaining the small size and strong surface plasmon resonance. For example, metal-dielectric-metal (MDM) hybrid nanostructures have been synthesized [23] and studied theoretically [5, 59, 92] in recent years, with excellent results (Fig. 3.12). Similarly, double concentric nanoshells (DCN), consisting of two concentric metallic nanoshells, have also been analyzed [59, 60] (Fig. 3.13) and fabricated [4, 6]. The advantage of these multilayered structures

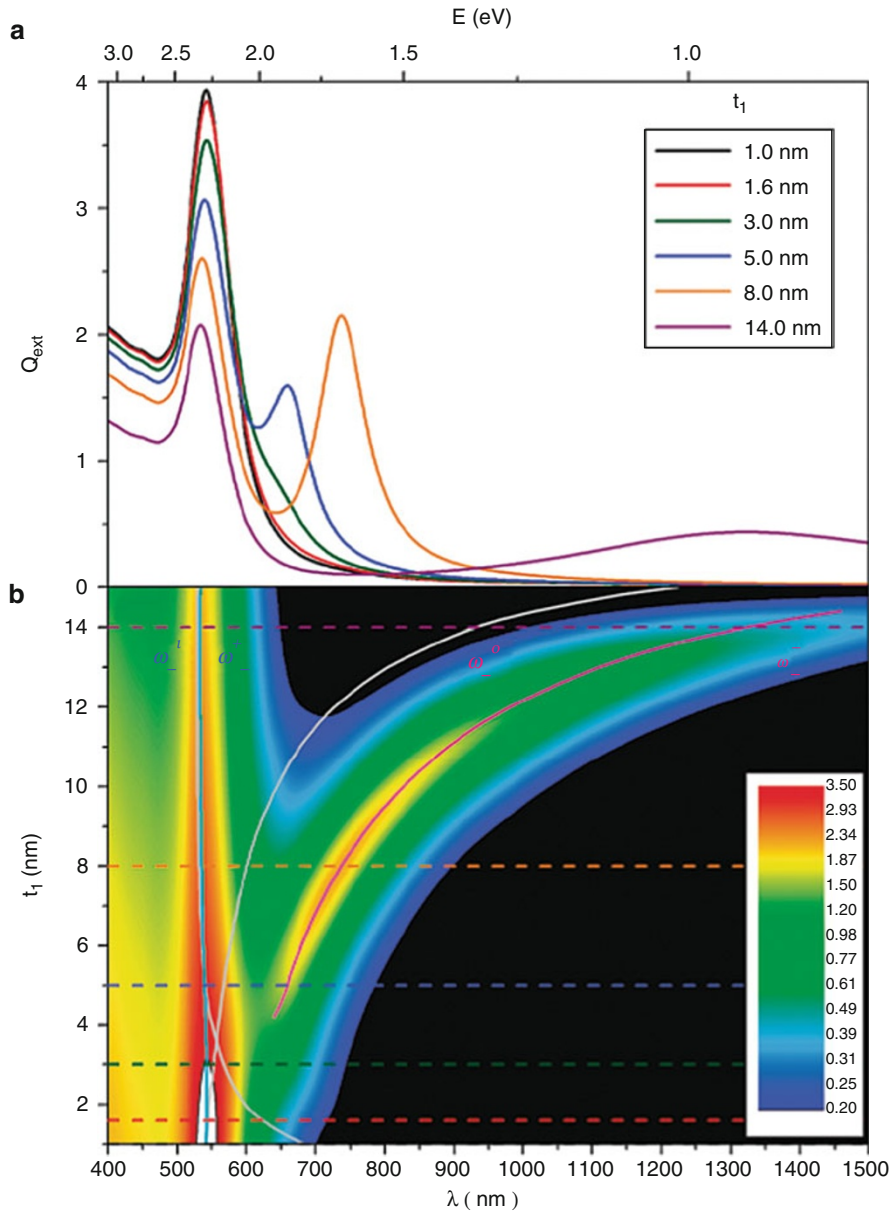
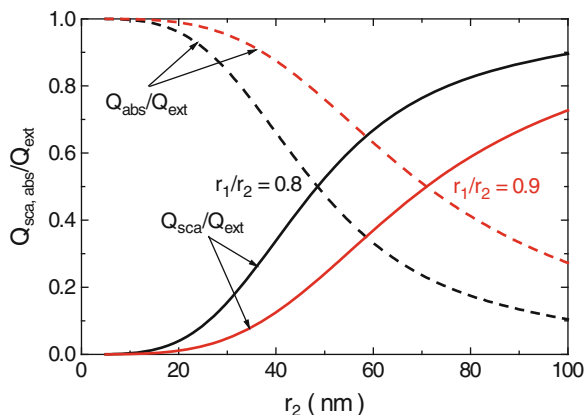


Fig. 3.13 Simulated extinction efficiency for a DCN, having $t_0 = t_2 = 5$ nm, while t_1 and t_3 are varied ($t_1 = 1, 2, \dots, 15$ nm; $t_3 = 16$ nm $- t_1$) simultaneously. For clarity, Q_{ext} is presented for some selected values of t_1 (a) and for the whole interval (b) [60]

Fig. 3.14 Calculated absorption (*dashed lines*) and scattering (*solid lines*) ratios, for gold nanoshells with fixed core-to-shell ratios of 0.8 (*black*) and 0.9 (*red*). For core-to-shell ratios of 0.8 and 0.9, the absorption and scattering efficiencies are almost equal for outer radii of ca. 50 and 70 nm, respectively. The efficiency ratios were calculated at the SPR maximum



over nanoshells comes from the extra SPR tunability provided by the additional layers. Therefore, the size of the particles can be further reduced without affecting their optical properties.

$Q_{\text{abs}}/Q_{\text{sca}}$ Ratio

In addition to spectral tunability, the absorption to scattering ratio of nanoshells can also be tuned by changing their outer radius (r_2). For smaller nanoshells, absorption dominates scattering, whereas for larger nanoshells the opposite is true. In between these two extremes, the contributions of absorption and scattering to total extinction can be controlled at will, depending on the total radius and on the core-to-shell ratio (Fig. 3.14). It is therefore possible to design nanoshells tailored for either diagnosis or therapy, where high scattering efficiencies facilitate scattering-based imaging and high absorption efficiencies facilitate photothermal therapy. In resume, by appropriately choosing the dimensions of r_1 and r_2 , the position of the extinction peak and the relative amounts of absorption and scattering can be selected across a wide range of wavelengths. This geometrical tunability is an outstanding property. In contrast, a large number of conventional organic dyes would be necessary to cover the same wide spectral range [24].

Near-Field Enhancement

Metallic nanoparticles (including nanoshells) exhibit another unique property. They efficiently concentrate the incident electromagnetic radiation into the near-field region close to their surfaces [93–95]. For example, Jackson et al. [96] and Averitt et al. [28] have predicted near-field enhancements ($|\mathbf{E}|/|\mathbf{E}_0|$, being \mathbf{E} and \mathbf{E}_0 the local and incident field, respectively) of around 30 and 3 for silver and gold nanoshells, respectively.

Hooshmand et al. [20], on the other hand, investigated systematically the effect of combining a nanoshell with a spheroid within the same nanostructure (i.e., a nanorice). They found that the plasmonic field enhancement is an order of magnitude larger for gold spheroidal nanoshells of aspect ratio 4 as compared to

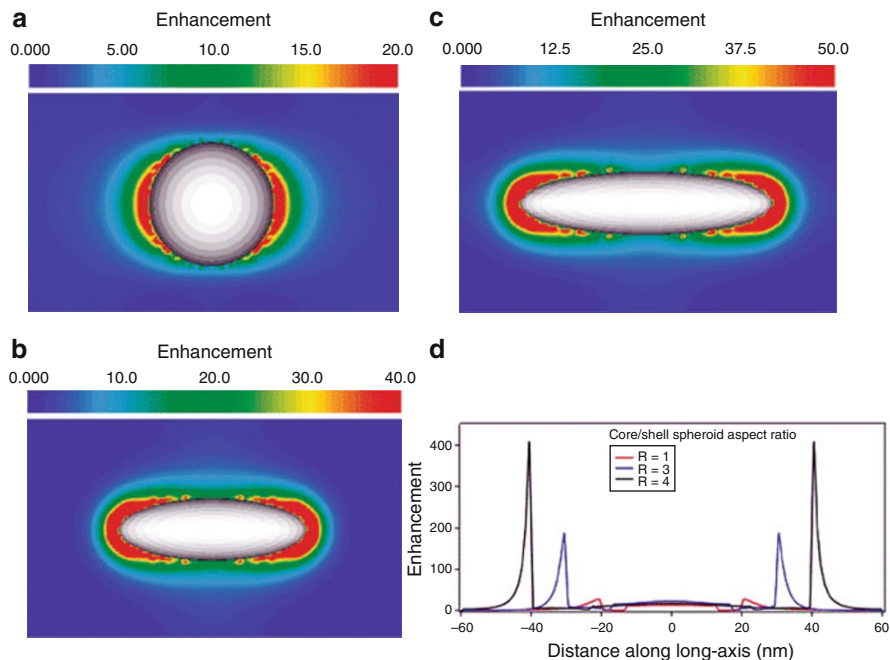


Fig. 3.15 Near-field enhancement in the vicinity of a spheroidal silica core-gold nanoshell as a function of the spheroidal aspect ratio for (a) a nanoshell with an aspect ratio of 1, an outer diameter of 40 nm, and a shell thickness of 7 nm; (b) a spheroidal nanoshell with an aspect ratio of 3, an outer dimension of 60 nm, and a shell thickness of 12 nm along the long axis; and (c) a spheroidal nanoshell with an aspect ratio of 4, an outer dimension of 80 nm, and a shell thickness of 16 nm along the long axis. (d) Line profile of the field enhancement along the long axis of the spheroid for all three aspect ratios [20]

spherical nanoshells of the same material (Fig. 3.15). Finally, Peña-Rodríguez and Pal [97] studied the plasmonic behavior of incomplete gold nanoshells, finding that during the initial stages of formation, well-separated, noninteracting metallic nanoparticles at the surface of a dielectric core behave like isolated particles, but intense and irregular local electric fields (with prominent hot spots that exhibit enhancements as high as 60) are created when the number of metallic spheres increases. Such enhancements are very important for applications like surface-enhanced Raman scattering (see Sect. 5.2.1) (Fig. 3.16) [98].

5.2 Applications

5.2.1 Surface-Enhanced Raman Scattering (SERS)

The first application of (gold) nanoshells in SERS was reported by Oldenburg et al. [98]. In this study, significant SERS signal was observed for p-mercaptoaniline (p-MA) in solution using gold nanoshells with plasmon resonance peak tuned to lie

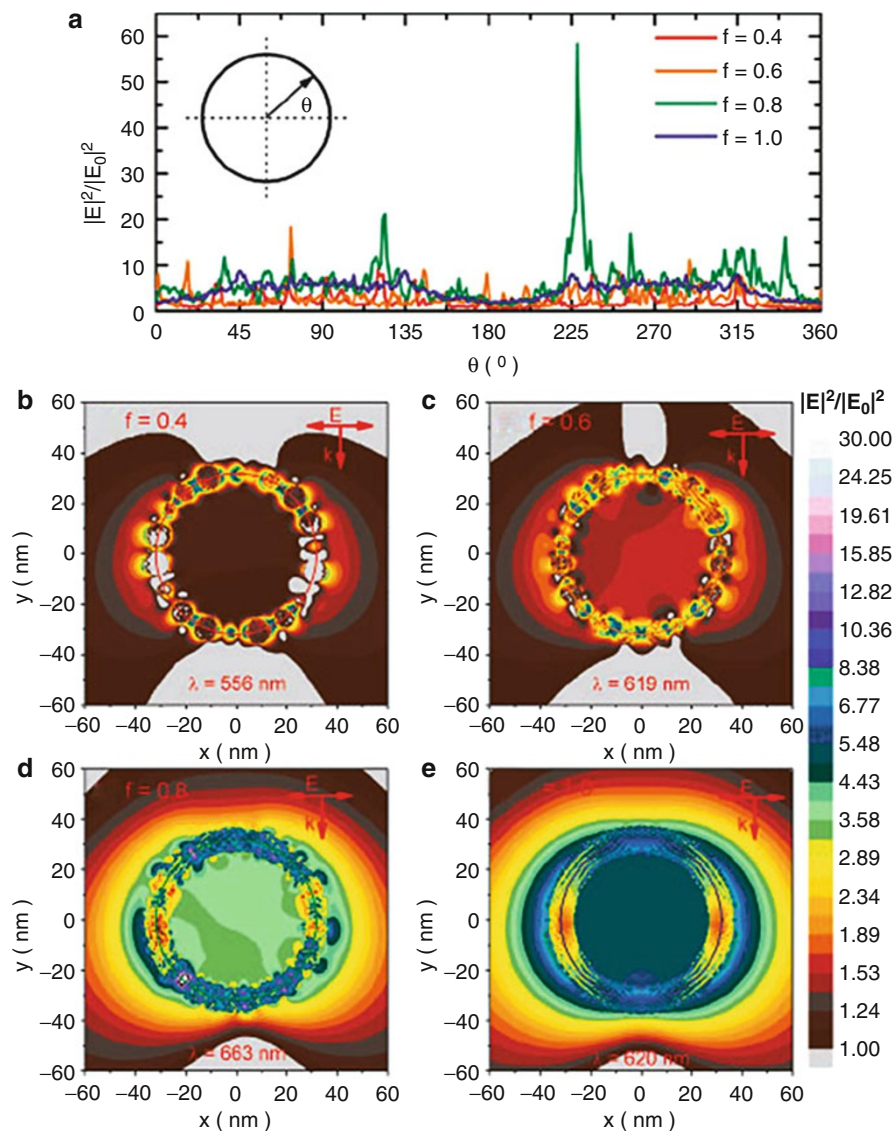


Fig. 3.16 Near-field contour plots in the section plane for some incomplete gold nanoshells. The structures shown have filling fractions of (b) 0.4, (c) 0.6, (d) 0.8, and (e) 1.0. (a) The field profiles through the middle of the metallic shell (marked with *solid lines* in the *contour plots*) are also shown, for clarity [97]

at the wavelength ($1.06 \mu\text{m}$) of the excitation source. The strongest Raman enhancements were obtained when enough gold was deposited on the silica cores to form a nearly complete metal shell. The SERS signal was found to be produced by two different factors: the local enhancement of the dielectric field via the

plasmon resonance of the nanostructure and the enhancement due to the localized regions of high field intensity provided by the nearly completed gold shell. A comparison between the SERS enhancements on complete nanoshell structures indicated the relative contribution of these two effects.

Silver nanoshells, owing to their intense SPR, are better SERS substrates than their gold counterparts, as has been observed by Jackson et al. [96]. They demonstrated that the variations of core diameter and shell layer thickness of a metallic nanoshell can tune the local surface electromagnetic field of the nanoparticle in a controlled manner, resulting in local field enhancements ($|E|/|E_0|$) of up to 30. Effective SERS enhancements of the order of 10^6 were obtained for these nanoshells in aqueous solution, which correspond to absolute enhancements $\sim 10^{12}$ when reabsorption of Raman emission by nearby nanoparticles is taken into account. Aggregates of composite Au/Ag nanoshells, fabricated on nanosized silica spheres by an aggregation-based method, also exhibited excellent optical properties, and their utility as substrates for surface-enhanced Raman scattering was demonstrated by Lu and coworkers [99]. Similarly, Jackson and Halas [100] found that SERS enhancements on Au and Ag nanoshell films are dramatically different from those observed on colloidal aggregates, measuring SERS enhancements as large as 2.5×10^{10} on Ag nanoshell films for the nonresonant molecule *p*-mercaptoaniline.

Goude and Leung [101] have applied the Gersten-Nitzan model to study the surface-enhanced Raman scattering from a molecule adsorbed on a spherical metallic nanoshell. They concluded that the nonlocal effects can be significant for very close molecule-shell distances and for shells with very small sizes and/or thickness, leading to smaller enhancement in general. On the other hand, Heck et al. [102] used SERS to provide the first direct evidence of the room-temperature catalytic hydrodechlorination of a chlorinated solvent through in situ the catalytic hydrodechlorination of 1,1-dichloroethene in H_2O . In this study, the authors employed Pd islands grown on Au nanoshell assembled films, exploiting the high enhancements and large active area of Au nanoshell SERS substrates, the transparency of Raman spectroscopy to aqueous solvents, and the catalytic activity enhancement of Pd by the underlying Au metal. The formation and subsequent transformation of several adsorbate species were observed.

Surface patterns of nanoshell arrays play an important role in diverse applications including SERS sensors, lithium-ion batteries, solar cells, and optical devices. Yang et al. [103] have described an innovative surface nanopatterning technique for realizing large-scale ordered arrays of spherical nanoshells with well-defined structures. Ag nanoshell arrays were fabricated using polystyrene sphere templates by an electrophoretic process in Ag colloidal solutions. With this fabrication process, it was possible to control various structural parameters of the nanoshell arrays, including the diameter, the surface roughness, and the inter-shell spacing. Tunable SERS and localized SPR of the nanoshell arrays were demonstrated by controlling the structural parameters. Moreover, Küstner et al. [104] have reported the silica encapsulation of a self-assembled monolayer (SAM) on metallic nanoparticles (Fig. 3.17). In this approach, the advantages of both the SAM and the silica shell

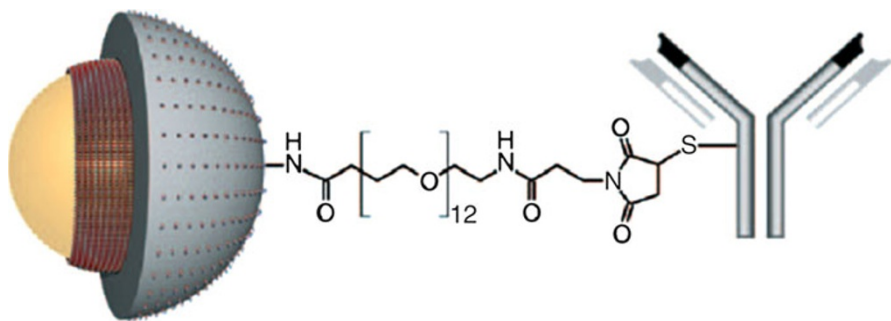


Fig. 3.17 Structure of silica-encapsulated and biofunctionalized SERS labels. *Left:* Gold/silver nanoparticle with a SAM of Raman label molecules (red) and a protective silica shell with amino groups (gray). *Middle:* heterobifunctional polyethylene glycol spacer. *Right:* monoclonal antibody for antigen recognition [104]

are integrated into a single functional unit. Using a SAM on gold/silver nanoshells optimized for red laser excitation, they found that these SERS labels give signals approximately 180 times more intense than those of other labels based on single gold particles.

Occurrence of SERS inside metal nanoshells was experimentally observed for the first time by Zhang and Guo [105]. They achieved giant enhancements of the order of 10^{11} – 10^{14} , solely due to the electromagnetic enhancement in the near-field. Meanwhile, Gellner et al. [106] have reported the optical properties and SERS efficiency of Au/Ag alloy nanoshells with different shell thickness. The relative SERS efficiency of the Au/Ag nanoshells was determined with a self-assembled monolayer of 4-mercaptobenzoic acid (MBA) as a probe molecule. They presented quantitative predictions of SERS efficiencies as high as 0.9, based on calculated Mie scattering intensities. Additionally, a qualitative analysis of their relative SERS efficiency was performed using two dominant Raman bands of MBA.

The application of gold nanoshells as SERS platform for intracellular sensing in NIH-3T3 fibroblast cells was studied by Ochsenkühn et al. [107], using MBA-functionalized nanoshells as a pH sensor. For this, they used 151 ± 5 -nm-sized solution-stable nanoparticles, finding the voluntary uptake of nanoshells by living cells. This controllable process was found to be independent of active cellular mechanisms, such as endocytosis. As a result, the cells showed no increase in necrosis or apoptosis. Nanoshell-based intracytosolic SERS spectra were measured using short acquisition times and low laser powers.

5.2.2 Surface-Enhanced Raman Optical Activity (SEROA)

Raman optical activity [108, 109] (ROA), which is defined as the difference between right- and left-circularly polarized Raman-scattering intensities, provides a spectroscopy that is sensitive to molecular chirality. The surface-enhanced version of ROA (SEROA) is even more sensitive and more selective than normal ROA spectroscopy. Acevedo et al. [110] have investigated SEROA theoretically for

molecules near a metal nanoshell. They calculated the SEROA excitation profiles and examined in detail the differential Raman scattering for a simple chiroptical model that provides analytical forms for the relevant dynamical molecular response tensors. This allowed a detailed investigation on the circumstances that simultaneously provide strong enhancement of differential intensities and selectivity to molecules with chirality. Moreover, Lombardini et al. [111] have examined SEROA in the same system for different experimental polarization schemes. Dual circular polarization strategies were found to have special advantages in these circumstances, and the corresponding excitation profiles for a simple chiroptical model were analyzed in detail to suggest preferred excitation wavelengths.

5.2.3 Medicine

Outstanding optical and chemical properties of metal (mainly gold) nanoshells make them interesting for medical applications [70], particularly in the areas of biomedical diagnostics, drug delivery, and thermal therapy of cancer [112, 113]. As the optical properties of these nanoshells are highly sensitive to the relative dimensions of the core and the shell, it is possible to design them to activate their plasmon frequencies in the near-infrared spectral range. In this energy range, the main components of body tissues, such as water, hemoglobin, and oxyhemoglobin, have weaker absorption (Fig. 3.11), making nanoshells useful for cancer treatment and/or detection [114]. Moreover, they can be tailored to either absorb or scatter EM radiation at this wavelength range, and, consequently, it can be controlled at will if the light is converted into heat or dispersed [115]. In the former case, the produced heat can be used to kill cancer cells or release drugs, while the scattering can be used to detect some types of malign cells.

In any case, nanoshells require adequate bio-conjugation for the attachment with biological cells. The bioconjugated nanoshells are then positioned specifically in the tumor to treat or detect the disease. Biomedical applications of nanoshells can be divided into two main categories: outside (i.e., *in vitro*) or inside (in *vivo*) the body. Among the former applications, we can find biosensors and biochips, which have been used to analyze various biological samples, particularly the blood, since 2002 [116]. For applications inside the body, researchers are working on the implementation of nanoshells tailored for enhanced thermal ablation of tumors, modulated drugs delivery, and cancer detection. In the following subsection, we will make a brief literature survey on the usage of nanoshells for medical applications.

Cancer Therapy

Complications associated with invasive malignant tumor excision have led to alternative treatment methods including chemotherapy, photodynamic therapy, and thermal coagulation. Metal nanoshells can provide a novel means for targeted photothermal therapy in tumor tissues, minimizing damage to the surrounding healthy tissues. Metal nanoshells have a strong tunable absorption, which can be placed in the near IR, where maximal penetration of light through biological tissues can be achieved. Moreover, when conjugated with a tumor-specific protein, these

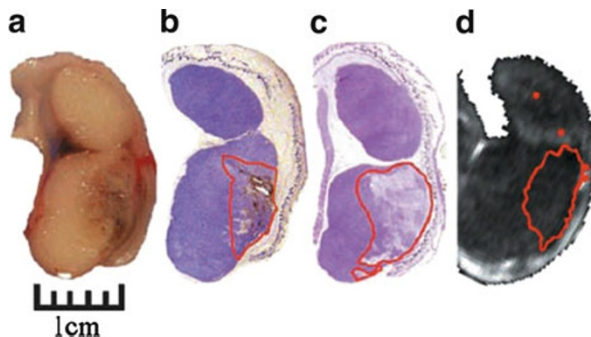


Fig. 3.18 (a) Gross pathology after in vivo treatment with nanoshells and NIR laser reveals hemorrhaging and loss of tissue birefringence beneath the apical tissue surface. (b) Silver staining of a tissue section reveals the region of localized nanoshells (outlined in red). (c) Hematoxylin/eosin staining within the same plane clearly shows tissue damage within the area occupied by nanoshells. (d) Likewise, MRTI calculations reveal an area of irreversible thermal damage of similar dimension to a, b, and c [91]

nanoshells could be systemically injected for the preferential attachment to the tumor sites. Up to date, cancer therapy using nanoshells has focused mainly in two directions: thermal ablation of tumors [91] and photothermally modulated drug delivery [117].

Thermal Ablation of Tumors

Phototherapy is a new therapeutic use of electromagnetic radiation for cancer treatment [118]. This type of therapy has the advantage of delivering a controlled amount of energy directly into the tumor mass. The laser energy delivered to the targeted tumors can induce localized photochemical, photomechanical, and photothermal reactions that kill the tumor cells [119]. However, the application of photothermal ablation is limited by the potential damage of the surrounding healthy tissues, as the heating from laser sources is nonspecific. Fortunately, nanoshells can be used to significantly enhance the efficiency of photothermal ablation because they exhibit a strong optical extinction at visible and near-infrared wavelengths, coming from the surface plasmon resonance. Moreover, these nanoparticles can be fabricated with well-defined core-shell ratio to absorb NIR light, resulting in a resonant and optimal transfer of thermal energies to the surrounding tissues. The absorption band in the NIR region is a desirable property because the normal tissues are relatively transparent to NIR light; thus, irradiation with NIR light causes minimal thermal injury to normal tissues [120]. Next, we will discuss the most significant advances that have been reported in the literature on the use of nanoshells for photothermal ablation of cancer cells.

Human breast carcinoma cells incubated with nanoshells in vitro were found to have undergone photothermally induced morbidity on exposure to NIR light (Fig. 3.18) [91]. In vivo studies under magnetic resonance guidance have also revealed that exposure of low doses of NIR light in solid tumors treated with

metal nanoshells attains average maximum temperatures capable of inducing irreversible tissue damage within 4–6 min. Tissues heated above the thermal damage threshold displayed coagulation, cell shrinkage, and loss of nuclear staining, which are indicators of irreversible thermal damage. Likewise, photothermally induced death of nanoshell-bound carcinoma cells *in vitro*, as well as *in vivo* [121] was demonstrated using an 821-nm diode laser combined with Au nanoshells fabricated to have their plasmon resonance at the same wavelength. Specific binding to tumor cells was achieved by conjugating antibodies against oncoproteins to nanoshells.

Laser-activated gold nanoshell-induced ablation has been found to be an effective and selective technique for both, an ectopic murine tumor model [122] and a subcutaneous murine colon tumor model [123]. In the former study, gold nanoshells of a total size of 110 nm with a 10-nm-thick metallic shell were designed to act as intense near-infrared absorbers, attaining temperatures up to 65.4 °C in the treated group which resulted in 93 % of tumor necrosis and regression for the high-dose-treated group. The ablation zone was sharply limited to the laser spot size. There was no difference in the size or tumor histology in control groups, indicating a benign course for near-infrared laser treatment alone. The second work relied on the enhanced permeability and retention effect, by which nanoscale materials are preferentially deposited into the tumors (as opposed to normal tissue) due to the leaky nature of tumor vessels. They reported an effective nanoshell-induced photothermal ablation of the tumor using polyethylene glycol-coated Au nanoshells (~130 nm in diameter) which accumulated in the tumor passively after intravenous injection.

This structure also proved effective to mediate a thermally induced modulation of tumor vasculature in experimental prostate tumors [124]. It was demonstrated that after passive extravasation and retention of the circulating nanoshells from the tumor vasculature into the tumor interstitium, the enhanced nanoshells absorption of near-infrared irradiation over normal vasculature can be used to increase tumor perfusion or shut it down at powers which result in no observable effects on tissue without nanoshells. The results indicated that nanoshell-mediated heating can be used to improve perfusion and subsequently enhance drug delivery and radiation effects or be used to shut down perfusion to assist in thermal ablative therapy delivery.

Enhanced targeted delivery of the nanoshells has also been demonstrated using a new class of molecular specific photothermal coupling agents based on hollow gold nanoshells (average diameter ~30 nm) covalently attached to monoclonal antibody directed at epidermal growth factor receptor (EGFR) [120]. The resulting anti-EGFR-NS exhibited excellent colloidal stability and efficient photothermal effect in the near-infrared region. EGFR-mediated selective uptake of anti-EGFR-NS in EGFR-positive A431 tumor cells but not IgG-NS control was shown *in vitro* by imaging scattered light from the nanoshells. Irradiation of anti-EGFR-NS treated A431 cells with near-infrared laser resulted in selective destruction of these cells. In contrast, cells treated with anti-EGFR-NS alone, laser alone, or IgG-NS plus laser did not show observable effect on cell viability. Using ¹¹¹In-labeled nanoshells, it was found that anti-EGFR-NS could be delivered to EGFR-positive tumors at 6.8 % ID/g,

and the microscopic image of excised tumor with scattering signal from nanoshells confirmed a preferential delivery of anti-EGFR-NS to A431 tumor compared with IgG-NS. The absence of silica core, the relatively small particle size and high tumor uptake, and the absence of cytotoxic surfactant required to stabilize other gold nanoparticles suggest that immuno-NS has the potential to extend to in vivo molecular therapy.

Mild-temperature hyperthermia generated by near-infrared illumination of gold nanoshell-laden tumors was reported to cause an early increase in tumor perfusion, reducing the hypoxic fraction of tumors [125, 126]. A subsequent radiation dose was used to induce vascular disruption with extensive tumor necrosis. The study determined that gold nanoshells sequestered in the perivascular space mediate these two tumor vasculature-focused effects to improve radiation response of tumors. This novel integrated antihypoxic and localized vascular disrupting therapy can potentially be combined with other conventional antitumor therapies. Similarly, local hyperthermia delivered by gold nanoshells plus radiation can eliminate radioresistant breast cancer stem cells [127]. In this work, it was confirmed that these cancer stem cells are responsible for accelerated repopulation in vivo and demonstrated that hyperthermia sensitizes this cell population to radiation treatment.

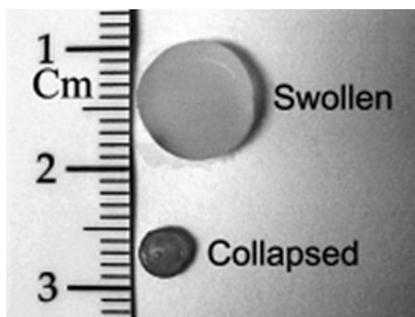
Active targeting of NSs to integrin $\alpha_v\beta_3$ increases its preferential accumulation in tumors and results in therapeutic nanoconstructs for effective cancer therapy [128]. Enzyme-linked immunosorbent assay (ELISA) and cell binding assay confirmed the binding affinity of NS-RGDfK to integrin $\alpha_v\beta_3$. Positron emission tomography/computed tomography imaging suggested that tumor targeting is improved by conjugation of NSs to cyclo(RGDfK) and peaks at ~ 20 h postinjection. In the subablative thermal therapy study, greater biological effectiveness of targeted NSs was implied by the greater degree of tumor necrosis.

Photothermally Modulated Drug Delivery

Another very important application of nanoshells that leverages the photothermal effect is the photothermally modulated drug delivery [129, 130]. Unfortunately conventional chemotherapeutic agents have poor specificity in reaching tumor tissues and are consequently restricted by dose-limiting toxicity. This limitation could be overcome using a combination of controlled release technology and targeted drug delivery. For this reason, a lot of recent efforts have been dedicated to the development of nanoscale delivery vehicles capable of controlling the release of chemotherapeutic agents directly inside the cancer cells [113]. This is achieved by combining a natural or synthetic polymer with a drug in such a way that the drug is encapsulated within the polymer system for subsequent release in a predetermined manner. One of the ways to obtain this goal is by means of photothermally modulated drug delivery. In this technique, optically active nanoshells are attached to thermally sensitive polymeric hydrogels, and the drug release is triggered with a laser emitting at the wavelength of the nanoshell SPR.

For example, composites of thermally sensitive hydrogels and optically active nanoparticles have been used to achieve significantly enhanced drug release in

Fig. 3.19 NIPAAm-co-AAm-nanoshell-composite hydrogels in the swollen and collapsed states. The change in volume is induced by heating [131]



response to light irradiation [117, 131]. Copolymers of N-isopropylacrylamide (NIPAAm) and acrylamide (AAm) exhibit a lower critical solution temperature (LCST) that is slightly above the body temperature. When the temperature of the copolymer exceeds the LCST, the hydrogel collapses (Fig. 3.19), causing a burst release of any soluble material held within the hydrogel matrix. Gold-gold sulfide nanoshells had been incorporated into poly(NIPAAm-co-AAm) hydrogels for the purpose of initiating a temperature change with light. The 1,064-nm light was absorbed by the nanoparticles, and converted to heat, leading to the release of methylene blue and proteins of varying molecular weights. Additionally, these nanoshell-composite hydrogels could release multiple bursts of protein in response to repeated near-IR irradiation. The very same composites were also found suitable for delivering controlled pulsatile doses of insulin in response to near-IR irradiation [132]. The activity of the released insulin was determined by measuring glucose uptake by adipocytes that had been exposed to photothermally released insulin. The released insulin did not show a loss in activity as compared to the positive control (insulin in saline), thus demonstrating transdermal photothermally modulated drug deliver in vitro.

Near-complete liposome release within seconds was demonstrated by irradiating hollow gold nanoshells with a near-infrared pulsed laser, overcoming their usual slow release of the encapsulated drug [133]. Different coupling methods, such as having the gold NSs tethered to, encapsulated within, or suspended freely outside the liposomes, were tested, finding that all triggered liposome release but with different levels of efficiency. Microbubble formation and collapse due to the rapid temperature increase of the NS, resulting in liposome disruption, was suggested as the underlying content release mechanism.

Nanoshell-composite hydrogels have also been used to develop a photothermal modulated drug delivery system [134]. SiO₂-Au nanoshells of varying concentrations have been embedded within temperature-sensitive *N*-isopropylacrylamide-co-acrylamide (NIPAAm-co-AAm) hydrogels. The resulting composites had the extinction spectrum of the SiO₂-Au nanoshells in which the hydrogels collapsed reversibly in response to temperature (50°C) and laser irradiation. The degree of collapse of the hydrogels was controlled by the laser fluence as well as the concentration of SiO₂-Au nanoshells. Modulated drug delivery profiles for

methylene blue, insulin, and lysozyme were achieved by irradiation of the drug-loaded nanoshell-composite hydrogels, revealing that drug release depends on the molecular weight of the therapeutic molecules. Similarly, a drug-loaded structure comprising a PEGylated (PEG = polyethylene glycol) gold nanoshell on silica nanorattle spheres was demonstrated to obtain combined remote-controlled photothermal therapy with modulated drug delivery [135]. Tumor cells were killed with higher efficacy and less toxicity than the free drug.

Tissue Welding

Gold nanoshells with peak extinction matching the NIR wavelength of the exciting laser also proved to be good exogenous NIR absorbers to facilitate NIR laser-tissue welding [114]. Goblin et al. have performed the optimization work on ex vivo muscle samples and then translated into testing in an in vivo rat skin wound-healing model. Mechanical testing of nanoshell-solder welds in muscle revealed successful fusion of tissues with tensile strengths of the weld site equal to the uncut tissue. No welding was accomplished with this light source when using solder formulations without nanoshells. Mechanical testing of the skin wounds showed sufficient strength for closure and strength increased over time. Histological examination showed good wound-healing response in the soldered skin. Notably, the healing results were similar to the suture-treat control group until day 5, after which healing was shown to be better in the suture group.

Bio-sensing and Imaging

As important as the treatment of tumors is their detection. Thanks to its versatility and low toxicity, nanoshells have also found wide applications in this field. For instance, bioconjugated nanoshells have been used as contrast agents, to detect and image individual cancer cells in vitro and solid tumors in vivo. In this case, one attempts to maximize the scattering of light rather than the absorption, which allows the sensing and/or imaging of tumors, facilitating its detection.

Bio-sensing

Potential applications of NSs in bio-sensing [116, 136] arise from the dependence of their surface plasmon resonance frequency on the refractive index of surrounding environment [70]. For sensing applications, a high sensitivity of the SPR frequency to the change in the refractive index of the surroundings ($\Delta\lambda_{SPR}/\Delta n_m$) is required. Sun and Xia [116, 137] have shown that gold nanoshells are more sensitive than solid nanospheres to the changes in refractive index of the surrounding environment (306.6 and 65.5 nm/RIU, respectively) and that the observed peak shift varies linearly with n_m (Fig. 3.20). Similar results were obtained by Tam et al. [138], who could measure sensitivities of up to $\Delta\lambda_{SPR}/\Delta n_m = 555.4$ nm/RIU. In this subsection, we will do a brief literature survey on how this optical sensitivity to the surrounding environment exhibited by nanoshells has been exploited to detect biomarkers in simple absorbance assays [16, 139].

A rapid immunoassay capable of detecting analyte within complex biological media without any sample preparation has been demonstrated [16, 140, 141].

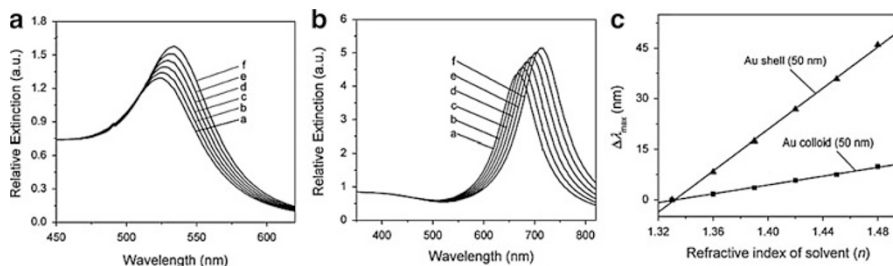


Fig. 3.20 Extinction coefficients computed for (a) a gold solid colloid with a diameter of 50 nm and (b) a gold nanoshell with a diameter of 50 nm and wall thickness of 4.5 nm. In simulation, the gold nanostructures are surrounded by solvents with increasing refractive indices: $n = 1.33$ (water), 1.36, 1.39, 1.42, 1.45, and 1.48. (c) Plots of the dependence of peak shift ($\Delta\lambda_{\text{SPR}}$, relative to the peak position calculated for water with $n = 1.33$) on the refractive index of surrounding medium. The sensitivity factors, $\Delta\lambda_{\text{SPR}}/\Delta n_m$, were 306.6 and 65.5 nm/RIU for gold nanoshell and 50-nm solid colloids, respectively. The interiors of these gold nanoshells were assumed to be filled by the external solvent [116]

This was accomplished using gold nanoshells as an immunoassay substrate. Near-infrared resonant gold nanoshells were labeled with antibodies specific to rabbit IgG analyte. Addition of analyte induced aggregation of antibody-nanoshell conjugates, causing a decrease in the SPR intensity. Successful detection of immunoglobulins was achieved in saline, serum, and whole blood. This simple immunoassay proved capable of quantitative detection of analyte within 10-30 min with sensitivities below 1 ng/mL. McFarland and Van Duyne [13] have used dark-field optical microscopy to demonstrate the localized surface plasmon resonance λ_{max} response of individual Ag nanoparticles and the formation of a monolayer of small-molecule adsorbates. They showed that the adsorption of fewer than 6×10^4 1-hexadecanethiol molecules on single Ag nanoparticles results in a localized surface plasmon resonance shift of 40.7 nm. Additionally, they found that the kinetics of the single nanoparticle response was comparable to that of other real-time sensor technologies.

Mie theory and the discrete dipole approximation method were used to calculate absorption, scattering efficiencies, and optical resonance wavelengths for three classes of nanoparticles commonly used for biological and cell imaging applications: gold nanospheres, silica-gold nanoshells, and gold nanorods [115]. In particular, gold nanoshells were found to have optical cross sections comparable to or even higher than nanospheres made of the same metal with the added advantage that their optical resonances lay favorably in the near-infrared region. The resonance wavelength could be rapidly increased by either increasing the total nanoshell size or increasing the ratio of the core-to-shell radius. The total extinction of nanoshells exhibits a linear dependence on their total size; however, it is independent of the core/shell radius ratio. It has also been found that the relative scattering contribution to the extinction can be rapidly raised by increasing the nanoshell size or decreasing the ratio of the core/shell radius.

Silica-gold nanoshells have also been used as solid-phase dot immunoassay [142, 143]. The principle of this assay is based on staining of a drop (1 μl) analyte on a nitrocellulose membrane strip by using silica-gold nanoshells conjugated with biospecific probing molecules. Experimental example was human IgG (hIgG, target molecules) and protein A (probing molecules). For 15-nm colloidal gold conjugates, the minimal detectable amount of hIgG was about 4 ng, but for nanoshell conjugates (silica core diameter of 70 nm and gold outer diameter of 100 nm), the detection sensitivity increased to about 0.5 ng. This finding has been explained by the difference in the monolayer particle extinction. Additionally, the optical mechanisms behind the efficiency of nanoparticle-labeled dot immunoassay have been addressed, both, theoretically and experimentally [144]. The experimental verification was performed with functionalized 15-nm colloidal gold nanospheres and silica-gold nanoshells. Three types of NSs, with silica core diameters of 100, 140, and 180 nm and a gold shell thickness of about 15 nm, were studied. A normal rabbit serum (the target IgG molecules) and sheep antirabbit antibodies (the probing molecules) were used as a biospecific model. It was found [139] that the minimal detection limit for IgG target molecules improves from 15 ng for 15-nm colloidal gold particles to around 0.25 ng in the case of 180/15-nm NSs and up to 0.5–1.0 ng for 100/15 and 140/15-nm NSs.

In yet another study, gold nanoshells were used as effective signal transducers in whole blood. First, NS self-assembled monolayers (SAMs) were formed on the surface of transparent glasses modified with 3-aminopropyltrimethoxysilane (APTES) [139]. Afterward, NS SAMs were modified with cystamine and biotin-NHS (N-hydroxysuccinimide) and used as a novel optical biosensor for real-time detection of streptavidin-biotin interactions in diluted human whole blood within short assay time, without any sample purification/separation. It has been shown that this biosensor featured a low detection limit $\sim 3 \mu\text{g/mL}$ and a wide dynamic range $\sim 3\text{--}50 \mu\text{g/mL}$.

Gold precursor composites, preadsorbed onto the surface of ITO substrates, were also used successfully as nanoprobess in an antioxidant capacity assay [145]. Nanoshell precursor composites were enlarged to varying degrees with the treatment of modified electrodes immersed in the gold nanoparticle growth solution containing different phenolic acids. Obtained results revealed that the higher capacity of phenolic acid to reduce AuCl_4^- to Au^0 resulted in the intensified localized SPR features and reduced cathodic currents. The optical and electrochemical results could be used to evaluate the antioxidant capacity of phenolic acids with this simple method. Similarly, a series of phenolic acids were also tested for their ability to scavenge hydrogen peroxide (H_2O_2) by using a novel enzyme-free, spectrophotometry assay [146]. Gold nanoshell precursor composites were used as optical nanoprobess. This approach was based on the H_2O_2 -induced growth of gold NSs. The addition of phenolic acids inhibits the formation of complete gold NSs, and the corresponding peak wavelength changed accordingly, acting as an optical signature. Caffeic acid was found to be the most efficient H_2O_2 -scavenger with its H_2O_2 -scavenging activity being $125 \times 10^{-3} \mu\text{M}^{-1}$, whereas trans-cinnamic acid exhibited the weakest activity ($0.73 \times 10^{-3} \mu\text{M}^{-1}$).

Imaging

Optical imaging of tissues is a high resolution, noninvasive technique that has the potential to greatly contribute to cancer detection [30]. Unfortunately, these technologies are often limited by the inherently weak optical signals of endogenous chromophores and the subtle spectral differences of normal and affected tissues. This limitation can be overcome by using exogenous contrast agents, designed to probe the molecular specific signatures of cancer, which improve the detection limits and clinical effectiveness of optical imaging [147]. In recent years, nanoshells have been increasingly used for this task, due to their outstanding optical properties.

Imaging of tumors has been achieved by using diffuse optical spectroscopy (DOS) for the noninvasive measurement of gold nanoshell concentrations in tumors of live mice [148, 149]. In this study, the diffuse optical spectra (500-800 nm) were measured using an optical fiber probe placed in contact with the tissue surface. In vitro studies were performed on tissue phantoms illustrating an accurate measurement of silica-gold nanoshell concentration within 12.6 % of the known concentration. Subsequent in vivo studies were performed on a mouse xenograft tumor model. DOS spectra were measured at preinjection, immediately after injection, and at 1 and 24 h postinjection times. The nanoshell concentrations were verified using neutron activation analysis.

The effective use of gold nanoshells as a contrast agent for optical coherence tomography (OCT) may be hampered by the delivery of a wrong dose resulting in unwanted signal attenuation. A recent study has examined how the changes in the scattering coefficient (μ_s) due to concentration variations affect the OCT image and defined a dose range that would result in optimal values of μ_s to maintain an acceptable signal attenuation level [150]. The results obtained by Kah et al., using 81-nm-radius silica core and 23-nm shell thickness revealed that an increase in μ_s not only enhances the OCT signal near the surface but also attenuates the signal deeper into the sample. It was found that a concentration range of $5.6 \times 10^9 < c < 2.3 \times 10^{10}$ particles/mL provides adequate signal enhancement near the surface without severely compromising the imaging depth due to signal attenuation. Finally, the extraction of μ_s from the OCT signal to estimate the gold nanoshells' concentration in vivo has also been demonstrated. The estimated concentration of 6.2×10^9 particles/mL in a mouse tumor after intravenous delivery lies within this concentration range to effectively enhance the tumor imaging.

The in vivo control of optical contrast in a mouse tumor model with gold nanoshells as contrast agent has been examined [151]. Gold nanoshells were administered into mice, with varying injected dosage and particle surface parameters. The results reasserted that a high concentration of gold nanoshells in tumor only enhances the OCT signal near the tissue surface while significantly attenuating the signal deeper into the tissue. However, with an appropriate dosage, intravenous (IV) delivery of gold nanoshells allows a moderate concentration of 6.2×10^9 particles/mL in tumor to achieve a good OCT signal enhancement with minimal signal attenuation at higher depths. An increase in the IV dosage of gold nanoshells revealed a corresponding nonlinear increase in their tumor concentration.

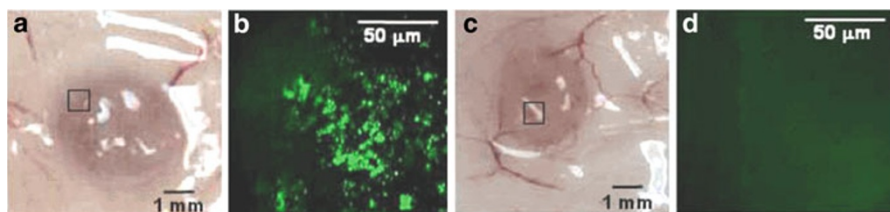


Fig. 3.21 Standard white light images and two-photon-induced photoluminescence (TPIP) images from subcutaneous tumors. (a), (c) White light images of tumor with and without nanoshells. (b), (d) TPIP images from tumors with and without nanoshells [152]

The fractional concentration could be improved with the use of antiepidermal growth factor receptor (EGFR) surface functionalization, which also reduced the time required for tumor delivery from 6 to 2 h.

Likewise, 3D microscopic imaging of gold nanoshells in tumors has been achieved using two-photon-induced photoluminescence [152–155]. This study took advantage of a new photo-physical property of nanoshells, whereby these particles glow brightly when excited by near-infrared light. Specifically, it was demonstrated that NSs excited at 780 nm produce strong two-photon-induced photoluminescence (TPIP, Fig. 3.21). The luminescence brightness of NSs was characterized and compared to that of fluorescein-labeled fluorescent beads (FB), finding that the former are 140 times brighter than the latter. 3D distribution of gold NSs targeted to murine tumors was imaged to demonstrate the potential application of this bright TPIP signal for biological imaging.

Gold NSs can be used as exogenous contrast agents for enhanced visualization of tumors using narrow band imaging (NBI) [156, 157]. NBI takes advantage of the strong NIR absorption of NSs to distinguish between blood and nanoshells in the tumor by imaging in narrow wavelength bands in the visible and NIR, respectively. First, the optimum wavelengths to enhance contrast between blood and NSs were determined using tissue-simulating phantoms. Then, these optimum wavelengths were used for ex vivo imaging of tumors extracted from human colon cancer xenograft-bearing mice injected with gold NSs. Systemically, delivered NSs accumulated passively in tumor xenografts due to the enhanced permeability and retention effects. Ex vivo NBI of tumor xenografts demonstrated tumor-specific heterogeneous distribution of NSs, with a clear distinction from the tumor vasculature.

The radiolabeling of gold nanoshells for positron emission tomography/computed tomography (PET/CT) imaging in rat tumor model has also been reported. For this purpose, the radionuclide ^{64}Cu was attached to the NSs via a conjugation method. In a first study [158], the resulting conjugates showed good labeling efficiency and stability in PBS and serum. The pharmacokinetics of ^{64}Cu -NS and the controls (^{64}Cu -DOTA and ^{64}Cu -DOTA-PEG2K) were determined in nude rats with a head and neck squamous cell carcinoma (HNSCC) xenograft by radioactive counting. In vivo distribution of ^{64}Cu -NSs and the controls in the tumor-bearing rats were monitored at various time points after their intravenous

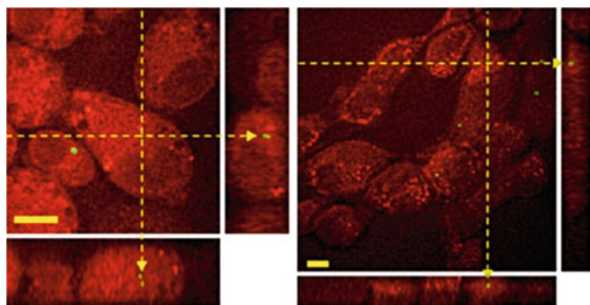


Fig. 3.22 Spatial distribution of gold NSs in live cultures of RAW 264.7 (*left*) and A431 (*right*). *Red contrast* corresponds with forward-detected CARS signal with pump and Stokes wavelengths tuned to excite the CH₂ resonance (*red*). *Green signal* corresponds with gold NS signal. Both bars represent 10 μm [159]

injection using PET/CT imaging. Obtained results showed accumulation of ⁶⁴Cu-NSs in the tumors and other organs with significant difference from the controls. The organ biodistribution of rats at 46 h postinjection was analyzed by radioactive counting and compared between the ⁶⁴Cu-NS and the controls. Different clearance kinetics was indicated. Neutron activation analysis (NAA) of gold concentration was performed to quantify the amount of NSs in major tissues of the dosed rats, and the obtained results revealed similar distributions. Overall, PET images using ⁶⁴Cu had good resolution and therefore can be further applied to guide photothermal treatment of cancer. *In vivo* biodistribution and tumor specificity were analyzed in a similar study [128], using ⁶⁴Cu-radiolabeled untargeted and targeted NSs in live nude rats bearing HNSCC xenografts. ELISA and cell binding assay confirmed the binding affinity of NS-RGDfK to integrin α_vβ₃. PET/CT imaging suggested that tumor targeting is improved by conjugation of NSs to cyclo(RGDfK) and peaks at ~20 h postinjection.

Finally, plasmon-enhanced four-wave mixing microscopy combined with coherent anti-Stokes Raman scattering (CARS) microscopy has been used to visualize the distribution of 75-nm-radius gold NSs within live cells (Fig. 3.22) [159]. It was found that living cells containing plasmonic nanoshells could be exposed up to 2.5 mJ with no detectable photothermally induced necrosis. In contrast, above this irradiation energy threshold, cell death occurs, which is linearly proportional to the laser power. The majority of the detected NS signals were through plasmon-enhanced four-wave mixing process, along the epi-direction with the incident lasers tuned to the silent region of the Raman spectrum. Then, the distribution of NSs inside live cells was visualized by combining the epi-detected signal with the forward-detected CARS at the CH₂ resonance.

5.2.4 Photonics

Colloidal particles can be assembled to form a two- or three-dimensional crystal lattice with long-range periodicity, known as photonic bandgap materials. The behavior of photons in these materials is equivalent to that of electrons in

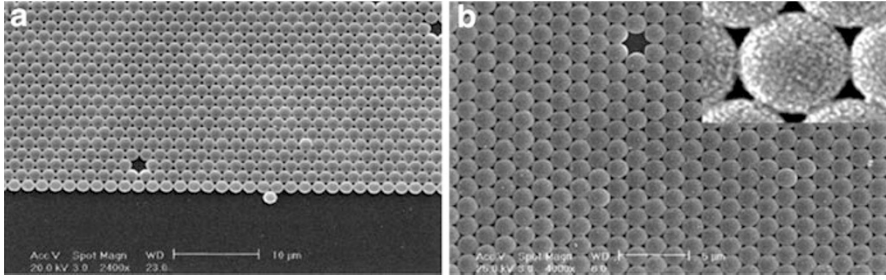


Fig. 3.23 (a) SEM image of a 2D colloidal crystal template composed of PS beads (diameter of 1,600 nm). (b) SEM image of the resultant 2D ordered array of metallodielectric composite microspheres. The inset in (b) shows the MD particles at a higher magnification. The silver shell thickness is about 45 ± 5 nm [160]

semiconductors. In this configuration, the gaps between the particles form a region of low refractive index, while the particles form a region of high refractive index. When photons are incident on these materials, they pass through regions with high and low refractive indices. For photons, this contrast in refractive index is similar to the periodic potential that an electron experiences while passing through a semiconductor. If the contrast in refractive index is large, then the photons are either totally reflected or confined inside the dielectric material. The colloidal crystal blocks wavelengths in the photonic bandgap while allowing other wavelengths to pass through. The photonic bandgap can be tuned by changing the size of the constituting particles.

Nanoshells are better suited than solid particles for this application because relative refractive index contrast in core and shell particles is higher [10]. Bandgap of such photonic crystals can be tuned from visible to IR range simply by changing index contrast [161]. For example, Zhan et al. [160] have studied the optical reflectance of a two-dimensional (2D) metallodielectric (MD) photonic crystal, composed of hexagonal array of close-packed silver shell polystyrene-core composite particles (Fig. 3.23). They observed a dramatic change in reflectivity behavior of the 2D MD film from a 2D colloidal crystal template and a homogeneous silver film. The phenomenon of strong reflectance bands of the 2D MD film was explained as a selective coupling of the incident light with surface plasmon of the 2D textured structure via the 2D grating.

Similarly, collective plasmonic modes in two- and three-dimensional periodic assemblies of metallic nanoshells were studied by means of full electrodynamic calculations [162, 163]. It was found that, in assemblies of metallic nanoshells, the plasmon resonances of the individual particles interact weakly between them and form narrow bands of collective plasmon modes that manifest themselves as resonance structures in corresponding transmission spectra and induce strong absorption. In contrast, for binary heterostructures, the collective plasmonic modes originating from the two building components coexist, leading to hybridization gaps, broadband absorption, and a rich structure of resonances over an extended range of frequencies.

5.2.5 Fano Resonances

Fano profiles are typical spectral features caused by the coupling of a discrete state with a continuum [164]. In particular, the all-plasmonic Fano resonance [25] was first described for a near-field coupled Au-Ag dimer, where the spectrally localized SPR of the silver nanoparticle (the discrete level) was coupled to the interband transitions of the gold nanoparticle (the continuum) [165]. In addition to fundamental scientific interests, Fano resonances in strongly coupled systems give rise to the so-called plasmon-induced transparency (PIT) [61], which is a phenomenon similar to the electromagnetically induced transparency, previously observed in atomic systems [166, 167]. In turn, PIT has a great potential for the fabrication of sub-wavelength waveguides, low-loss metamaterials, and chemical sensors [61, 168–171]. Therefore, it is not surprising that, apart from the original dimer, several plasmonic structures have been proposed as candidates for generating Fano resonances [61, 72, 168, 172, 173].

Fano resonances in modified MDM nanoshells (also referred as Fanoshells [174]) have been recently reported by Hu et al. [22] and Mukherjee et al. [61]. In these structures, the center of the metallic shell had been displaced with respect to the center of the metallic core. Then, the dipolar modes of the inner core interacted with quadrupolar and higher multipolar plasmon modes of the outer shell due to the symmetry breaking introduced by the displacement of the core, resulting in Fano interference. It was found that the resulting Fano resonance was almost isotropic (i.e., independent of the polarization of the incident light), opening the possibility of applying them as metamaterials.

6 Conclusions and Future Perspective

Research on metal nanoshells has had a short but intense life. The theoretical tools to calculate their optical properties existed since the 50s [45]. However, it was only in 1989 that Neeves and Birnboim [53] demonstrated, using theoretical calculations, that a composite spherical particle with a dielectric core and a metallic shell can produce SPR modes in a much larger range of wavelengths than solid ones. They predicted that those SPR wavelengths would be tunable by controlling the geometrical parameters of the core and shell. The first nanoshells, consisting of an Au₂S core surrounded by a gold shell, were synthesized a few years later by Zhou et al. [27] and allowed shifting the plasmon resonance peak from 520 nm (gold colloids) up to 900 nm. However, additional red-shifts were restricted by the chemistry of the synthesis reactions, which imposed a limit of around 40 nm on the maximum achievable size of nanoshells [9]. The process also produced large amounts of gold colloid as a secondary product, generating an additional absorption peak around 520 nm [9]. Most of the limitations of those first nanoshells were overcome by a new type of gold nanoshells, synthesized by Halas and coworkers [71]. The new method replaced the Au₂S core of the previous structure by monodisperse spherical silica particles, opening the possibility of much greater control over the spectral position of SPR in nanoshells [2].

After that, applications of nanoshells flourished. In 1999, Oldenburg et al. [98] demonstrated the use of nanoshells in surface-enhanced Raman scattering (SERS). A year later Sershen et al. [117] used them for photothermally modulated drug delivery. Sun and Xia [116] showed in 2002 that nanoshells are more sensitive than nanospheres to changes in the refractive index of the surrounding environment, opening the door to their use as sensors. Hirsh et al. [91] revealed its usefulness for thermal ablation of tumors in 2003. Goblin et al. [114] proved in 2005 that they can be good exogenous NIR absorbers to facilitate NIR laser-tissue welding. Last year (2010), Hu et al. [22] reported the appearance of Fano resonances in metal-dielectric-metal (MDM) nanoshells with the center of the metallic shell displaced with respect to the center of the metallic core.

Moreover, the methods of nanoshell synthesis have also been improved considerably, allowing an always-growing control over the morphology of the nanoshells that lead to several new variations such as the nanorice [19, 20] (ellipsoidal nanoshells) as well as nonconcentric [21, 22] and multilayered [6, 23] nanoshells. All of them have proved capable of increasing the upper limit of allowed red-shifts. However, despite all those advances made in the study of nanoshells, the possibilities of development are still very large. It is not hard to foresee that the current trend on nanoshell research will continue, achieving greater control over their morphology and size, while new applications appear and existing ones are improved. In the end, it will be possible to fabricate nanoshells with features tailored to the needs of each particular application.

References

1. Oldenburg SJ, Jackson JB, Westcott SL, Halas NJ (1999) Infrared extinction properties of gold nanoshells. *Appl Phys Lett* 75(19):2897–2899
2. Oldenburg SJ, Averitt RD, Westcott SL, Halas NJ (1998) Nanoengineering of optical resonances. *Chem Phys Lett* 288(2–4):243–247
3. Peña O, Pal U, Rodríguez-Fernández L, Crespo-Sosa A (2008) Linear optical response of metallic nanoshells in different dielectric media. *J Opt Soc Am B* 25(8):1371–1379
4. Radloff C, Halas NJ (2004) Plasmonic properties of concentric nanoshells. *Nano Lett* 4(7):1323–1327
5. Wu D, Liu X (2009) Tunable near-infrared optical properties of three-layered gold-silica-gold nanoparticles. *Appl Phys B Lasers Optics* 97(1):193–197
6. Prodan E, Radloff C, Halas NJ, Nordlander P (2003) A hybridization model for the plasmon response of complex nanostructures. *Science* 302(5644):419–422
7. Schwartzberg AM, Olson TY, Talley CE, Zhang JZ (2006) Synthesis, characterization, and tunable optical properties of hollow gold nanospheres. *J Phys Chem B* 110(40):19935–19944
8. Anker JN, Hall WP, Lyandres O, Shah NC, Zhao J, Van Duyne RP (2008) Biosensing with plasmonic nanosensors. *Nat Mater* 7(6):442–453
9. Averitt RD, Sarkar D, Halas NJ (1997) Plasmon resonance shifts of Au-coated Au₂S nanoshells: insight into multicomponent nanoparticle growth. *Phys Rev Lett* 78(22):4217
10. Kalele S, Gosavi SW, Urban J, Kulkarni SK (2006) Nanoshell particles: synthesis, properties and applications. *Curr Sci* 91(8):1038–1052
11. Sönnichsen C, Alivisatos AP (2005) Gold nanorods as novel nonbleaching plasmon-based orientation sensors for polarized single-particle microscopy. *Nano Lett* 5(2):301–304

12. Raschke G, Brogl S, Susha AS, Rogach AL, Klar TA, Feldmann J, Fieres B, Petkov N, Bein T, Nichtl A, Kurzinger K (2004) Gold nanoshells improve single nanoparticle molecular sensors. *Nano Lett* 4(10):1853–1857
13. McFarland AD, Van Duyne RP (2003) Single silver nanoparticles as real-time optical sensors with zeptomole sensitivity. *Nano Lett* 3(8):1057–1062
14. Xu H, Käll M (2002) Surface-plasmon-enhanced optical forces in silver nanoaggregates. *Phys Rev Lett* 89(24):246802
15. Allain LR, Vo-Dinh T (2002) Surface-enhanced Raman scattering detection of the breast cancer susceptibility gene BRCA1 using a silver-coated microarray platform. *Anal Chim Acta* 469(1):149–154
16. Hirsch LR, Jackson JB, Lee A, Halas NJ, West JL (2003) A whole blood immunoassay using Gold nanoshells. *Anal Chem* 75(10):2377–2381
17. Cui Y, Ren B, Yao J-L, Gu R-A, Tian Z-Q (2006) Synthesis of Ag_{core}-Au_{shell} bimetallic nanoparticles for immunoassay based on surface-enhanced Raman spectroscopy. *J Phys Chem B* 110(9):4002–4006
18. Premasiri WR, Moir DT, Klempner MS, Krieger N, Jones G, Ziegler LD (2005) Characterization of the surface enhanced Raman scattering (SERS) of bacteria. *J Phys Chem B* 109(1):312–320
19. Wang H, Brandl DW, Le F, Nordlander P, Halas NJ (2006) Nanorice: a hybrid plasmonic nanostructure. *Nano Lett* 6(4):827–832
20. Hooshmand N, Jain PK, El-Sayed MA (2011) Plasmonic spheroidal metal nanoshells showing larger tunability and stronger near fields than their spherical counterparts: an effect of enhanced plasmon coupling. *J Phys Chem Lett* 2(5):374–378
21. Wu Y, Nordlander P (2006) Plasmon hybridization in nanoshells with a nonconcentric core. *J Chem Phys* 125(12):124708
22. Hu Y, Noelck SJ, Drezek RA (2010) Symmetry breaking in gold-silica-gold multilayer nanoshells. *ACS Nano* 4(3):1521–1528
23. Xia X, Liu Y, Backman V, Ameer GA (2006) Engineering sub-100 nm multi-layer nanoshells. *Nanotechnology* 17(21):5435–5440
24. Erickson TA, Tunnell JW (2009) Gold nanoshells in biomedical applications. In: Kumar CSSR (eds) *Nanomaterials for the life sciences: mixed metal nanomaterials*, vol 3. Wiley-VCH, Weinheim, Germany, pp. 1–44.
25. Luk'yanchuk B, Zheludev NI, Maier SA, Halas NJ, Nordlander P, Giessen H, Chong CT (2010) The Fano resonance in plasmonic nanostructures and metamaterials. *Nat Mater* 9(9):707–715
26. Sattler KD (2010) *Nanomedicine and nanorobotics*. CRC Press, Boca Raton
27. Zhou HS, Honma I, Komiyama H, Haus JW (1994) Controlled synthesis and quantum-size effect in gold-coated nanoparticles. *Phys Rev B* 50(16):12052–12056
28. Averitt RD, Westcott SL, Halas NJ (1999) Linear optical properties of gold nanoshells. *J Opt Soc Am B* 16(10):1824–1832
29. Averitt RD, Westcott SL, Halas NJ (1998) Ultrafast electron dynamics in gold nanoshells. *Phys Rev B* 58(16):R10203
30. Loo C, Lin A, Hirsch L, Lee M-H, Barton J, Halas N, West J, Drezek R (2004) Nanoshell-enabled photonics-based imaging and therapy of cancer. *Technol Cancer Res Treat* 3(1):33–40
31. Westcott SL, Oldenburg SJ, Lee TR, Halas NJ (1998) Formation and adsorption of clusters of gold nanoparticles onto functionalized silica nanoparticle surfaces. *Langmuir* 14(19):5396–5401
32. Westcott SL, Oldenburg SJ, Lee TR, Halas NJ (1999) Construction of simple gold nanoparticle aggregates with controlled plasmon-plasmon interactions. *Chem Phys Lett* 300(5–6):651–655
33. Caruso F (2001) Nanoengineering of particle surfaces. *Adv Mater* 13(1):11–22
34. Shi W, Sahoo Y, Swihart MT, Prasad PN (2005) Gold nanoshells on polystyrene cores for control of surface plasmon resonance. *Langmuir* 21(4):1610–1617

35. Salgueiriño-Maceira V, Caruso F, Liz-Marzán LM (2003) Coated colloids with tailored optical properties. *J Phys Chem B* 107(40):10990–10994
36. Stöber W, Fink A, Bohn E (1968) Controlled growth of monodisperse silica spheres in the micron size range. *J Colloid Interface Sci* 26(1):62–69
37. Zhang J, Chen Z, Wang Z, Zhang W, Ming N (2003) Preparation of monodisperse polystyrene spheres in aqueous alcohol system. *Mater Lett* 57(28):4466–4470
38. Brinson BE, Lassiter JB, Levin CS, Bardhan R, Mirin N, Halas NJ (2008) Nanoshells made easy: improving Au layer growth on nanoparticle surfaces. *Langmuir* 24(24):14166–14171
39. Zhang J, Liu J, Wang S, Zhan P, Wang Z, Ming N (2004) Facile methods to coat polystyrene and silica colloids with metal. *Adv Funct Mater* 14(11):1089–1096
40. Lim YT, Park OO, Jung H-T (2003) Gold nanolayer-encapsulated silica particles synthesized by surface seeding and shell growing method: near infrared responsive materials. *J Colloid Interface Sci* 263(2):449–453
41. Peceros KE, Xu X, Bulcock SR, Cortie MB (2005) Dipole-dipole plasmon interactions in gold-on-polystyrene composites. *J Phys Chem B* 109(46):21516–21520
42. Zhang JH, Zhan P, Wang ZL, Zhang WY, Ming NB (2003) Preparation of monodisperse silica particles with controllable size and shape. *J Mater Res* 18(03):649–653
43. Yang W (2003) Improved recursive algorithm for light scattering by a multilayered sphere. *Appl Opt* 42(9):1710–1720
44. Mie G (1908) Beiträge zur optik trüber medien, speziell kolloidaler metallösungen. *Ann Phys* 330(3):377–445
45. Aden AL, Kerker M (1951) Scattering of electromagnetic waves from two concentric spheres. *J Appl Phys* 22(10):1242–1246
46. Wyatt PJ (1962) Scattering of electromagnetic plane waves from inhomogeneous spherically symmetric objects. *Phys Rev* 127(5):1837–1843
47. Wyatt PJ (1964) Scattering of electromagnetic plane waves from inhomogeneous spherically symmetric objects. *Phys Rev* 134(7A):AB1–AB1
48. Bhandari R (1985) Scattering coefficients for a multilayered sphere: analytic expressions and algorithms. *Appl Opt* 24(13):1960–1967
49. Wait J (1963) Electromagnetic scattering from a radially inhomogeneous sphere. *Appl Sci Res B* 10(5):441–450
50. Wait JR (1955) Scattering of a plane wave from a circular dielectric cylinder at oblique incidence. *Can J Phys* 33(5):189–195
51. Kim CS, Yeh C (1991) Scattering of an obliquely incident wave by a multilayered elliptical lossy dielectric cylinder. *Radio Sci* 26(5):1165–1176
52. Asano S, Yamamoto G (1975) Light scattering by a spheroidal particle. *Appl Opt* 14(1):29–49
53. Neeves AE, Birnboim MH (1989) Composite structures for the enhancement of nonlinear-optical susceptibility. *J Opt Soc Am B* 6(4):787–796
54. Bohren CF, Huffman DR (1998) Absorption and scattering of light by small particles. Wiley-Interscience, New York
55. Abramowitz M (1965) Handbook of mathematical functions. Dover, New York
56. Arfken GB, Weber HJ, Harris F (2005) Mathematical methods for physicists, 6th edn. Academic, San Diego
57. Kai L, Massoli P (1994) Scattering of electromagnetic-plane waves by radially inhomogeneous spheres: a finely stratified sphere model. *Appl Opt* 33(3):501–511
58. Prodan E, Nordlander P (2003) Structural tunability of the plasmon resonances in metallic nanoshells. *Nano Lett* 3(4):543–547
59. Peña-Rodríguez O, Pal U (2011) Enhanced plasmonic behavior of bimetallic (Ag-Au) multilayered spheres. *Nanoscale Res Lett* 6(1):279
60. Peña-Rodríguez O, Pal U (2010) Geometrical tunability of linear optical response of silica-gold double concentric nanoshells. *J Phys Chem C* 114(10):4414–4417

61. Mukherjee S, Sobhani H, Lassiter JB, Bardhan R, Nordlander P, Halas NJ (2010) Fanoshells: nanoparticles with built-in Fano resonances. *Nano Lett* 10(7):2694–2701
62. Rohde CA, Hasegawa K, Deutsch M (2006) Coherent light scattering from semicontinuous silver nanoshells near the percolation threshold. *Phys Rev Lett* 96(4):045503
63. Preston TC, Signorell R (2009) Growth and optical properties of gold nanoshells prior to the formation of a continuous metallic layer. *ACS Nano* 3(11):3696–3706
64. Lin Q, Sun Z (2011) Optical extinction properties of aggregated ultrafine silver nanoparticles on silica nanospheres. *J Phys Chem C* 115(5):1474–1479
65. Yee K (1966) Numerical solution of initial boundary value problems involving maxwell's equations in isotropic media. *IEEE Trans Antennas Propagation* 14(3):302–307
66. Purcell EM, Pennypacker CR (1973) Scattering and absorption of light by nonspherical dielectric grains. *Astrophys J* 186:705–714
67. Draine BT (1988) The discrete-dipole approximation and its application to interstellar graphite grains. *Astrophys J* 333:848
68. Draine BT, Flatau PJ (1994) Discrete-dipole approximation for scattering calculations. *J Opt Soc Am A* 11(4):1491–1499
69. Halas N (2005) Playing with plasmons: tuning the optical resonant properties of metallic nanoshells. *MRS Bull* 30(05):362–367
70. Kelly KL, Coronado E, Zhao LL, Schatz GC (2003) The optical properties of metal nanoparticles: the influence of size, shape, and dielectric environment. *J Phys Chem B* 107(3):668–677
71. Hu M, Chen J, Li Z-Y, Au L, Hartland GV, Li X, Marquez M, Xia Y (2006) Gold nanostructures: engineering their plasmonic properties for biomedical applications. *Chem Soc Rev* 35(11):1084
72. Peña-Rodríguez O, Pal U (2011) Au@Ag core-shell nanoparticles: efficient all-plasmonic Fano-resonance generators. *Nanoscale* 3(9):3609–3612
73. Prodan E, Nordlander P, Halas NJ (2003) Electronic structure and optical properties of gold nanoshells. *Nano Lett* 3(10):1411–1415
74. Johnson PB, Christy RW (1972) Optical constants of the noble metals. *Phys Rev B* 6(12):4370–4379
75. Palik ED (1997) Handbook of optical constants of solids. Academic, New York
76. Hao F, Nordlander P (2007) Efficient dielectric function for FDTD simulation of the optical properties of silver and gold nanoparticles. *Chem Phys Lett* 446(1–3):115–118
77. Vial A, Grimault A-S, Macías D, Barchiesi D, de la Chapelle ML (2005) Improved analytical fit of gold dispersion: application to the modeling of extinction spectra with a finite-difference time-domain method. *Phys Rev B* 71(8):085416
78. See KC, Spicer JB, Brupbacher J, Zhang D, Vargo TG (2005) Modeling interband transitions in silver nanoparticle-fluoropolymer composites. *J Phys Chem B* 109(7):2693–2698
79. Lee T-W, Gray S (2005) Subwavelength light bending by metal slit structures. *Opt Express* 13(24):9652–9659
80. Moskovits M, Srnová-Sloufova I, Vlckova B (2002) Bimetallic Ag-Au nanoparticles: extracting meaningful optical constants from the surface-plasmon extinction spectrum. *J Chem Phys* 116(23):10435–10446
81. Rakic AD, Djuricic AB, Elazar JM, Majewski ML (1998) Optical properties of metallic films for vertical-cavity optoelectronic devices. *Appl Opt* 37(22):5271–5283
82. Etchegoin PG, Le Ru EC, Meyer M (2006) An analytic model for the optical properties of gold. *J Chem Phys* 125(16):164705
83. Etchegoin P, Kircher J, Cardona M (1993) Elasto-optical constants of Si. *Phys Rev B* 47(16):10292–10303
84. Campoy-Quiles M, Heliotis G, Xia R, Ariu M, Pintani M, Etchegoin P, Bradley DDC (2005) Ellipsometric characterization of the optical constants of polyfluorene gain media. *Adv Funct Mater* 15(6):925–933

85. Leng J, Opsal J, Chu H, Senko M, Aspnes DE (1998) Analytic representations of the dielectric functions of materials for device and structural modeling. *Thin Solid Films* 313–314:132–136
86. Noguez C (2005) Optical properties of isolated and supported metal nanoparticles. *Opt Mater* 27(7):1204–1211
87. Ashcroft NW, Mermin ND (1976) *Solid state physics*, 1st edn. Brooks Cole, Philadelphia
88. Hamblin MR (2006) Mechanisms of low level light therapy. *Proc SPIE* 6140:614001
89. Stolik S, Delgado JA, Pérez A, Anasagasti L (2000) Measurement of the penetration depths of red and near infrared light in human “ex vivo” tissues. *J Photochem Photobiol B Biol* 57(2–3):90–93
90. Ntziachristos V, Ripoll J, Wang LV, Weissleder R (2005) Looking and listening to light: the evolution of whole-body photonic imaging. *Nat Biotechnol* 23(3):313–320
91. Hirsch LR, Stafford RJ, Bankson JA, Sershen SR, Rivera B, Price RE, Hazle JD, Halas NJ, West JL (2003) Nanoshell-mediated near-infrared thermal therapy of tumors under magnetic resonance guidance. *Proc Natl Acad Sci USA* 100(23):13549–13554
92. Hasegawa K, Rohde C, Deutsch M (2006) Enhanced surface-plasmon resonance absorption in metal-dielectric-metal layered microspheres. *Opt Lett* 31(8):1136–1138
93. Oldenburg SJ, Hale GD, Jackson JB, Halas NJ (1999) Light scattering from dipole and quadrupole nanoshell antennas. *Appl Phys Lett* 75(8):1063
94. Wang H, Fu K, Drezek RA, Halas NJ (2006) Light scattering from spherical plasmonic nanoantennas: effects of nanoscale roughness. *Appl Phys B Lasers Optics* 84(1):191–195
95. Chien W-Y, Szkopek T (2008) Multiple-multipole simulation of optical nearfields in discrete metal nanosphere assemblies. *Opt Express* 16(3):1820–1835
96. Jackson JB, Westcott SL, Hirsch LR, West JL, Halas NJ (2003) Controlling the surface enhanced Raman effect via the nanoshell geometry. *Appl Phys Lett* 82(2):257
97. Peña Rodríguez O, Pal U (2011) Enhanced plasmonic behavior of incomplete nanoshells: effect of local field irregularities on the far-field optical response. *J Phys Chem C* 115(45):22271–22275
98. Oldenburg SJ, Westcott SL, Averitt RD, Halas NJ (1999) Surface enhanced Raman scattering in the near infrared using metal nanoshell substrates. *J Chem Phys* 111(10):4729
99. Lu L, Zhang H, Sun G, Xi S, Wang H, Li X, Wang X, Zhao B (2003) Aggregation-based fabrication and assembly of roughened composite metallic nanoshells: application in surface-enhanced raman scattering. *Langmuir* 19(22):9490–9493
100. Jackson JB, Halas NJ (2004) Surface-enhanced Raman scattering on tunable plasmonic nanoparticle substrates. *Proc Natl Acad Sci USA* 101(52):17930–17935
101. Goude ZE, Leung PT (2007) Surface enhanced Raman scattering from metallic nanoshells with nonlocal dielectric response. *Solid State Commun* 143(8–9):416–420
102. Heck KN, Janesko BG, Scuseria GE, Halas NJ, Wong MS (2008) Observing metal-catalyzed chemical reactions in situ using surface-enhanced Raman spectroscopy on Pd-Au nanoshells. *J Am Chem Soc* 130(49):16592–16600
103. Yang S, Cai W, Kong L, Lei Y (2010) Surface nanometer-scale patterning in realizing large-scale ordered arrays of metallic nanoshells with well-defined structures and controllable properties. *Adv Funct Mater* 20(15):2527–2533
104. Küstner B, Gellner M, Schütz M, Schöppler F, Marx A, Ströbel P, Adam P, Schmuck C, Schlücker S (2009) SERS labels for red laser excitation: silica-encapsulated SAMS on tunable gold/silver nanoshells. *Angew Chem Int Ed* 48(11):1950–1953
105. Zhang P, Guo Y (2009) Surface-enhanced Raman scattering inside metal nanoshells. *J Am Chem Soc* 131(11):3808–3809
106. Gellner M, Küstner B, Schlücker S (2009) Optical properties and SERS efficiency of tunable gold/silver nanoshells. *Vibrat Spectros* 50(1):43–47
107. Ochsenkuhn MA, Jess PRT, Stoquert H, Dholakia K, Campbell CJ (2009) Nanoshells for surface-enhanced Raman spectroscopy in Eukaryotic cells: cellular response and sensor development. *ACS Nano* 3(11):3613–3621

108. Barron LD, Buckingham AD (1971) Rayleigh and Raman scattering from optically active molecules. *Mol Phys* 20(6):1111–1119
109. Barron LD, Zhu F, Hecht L, Tranter GE, Isaacs NW (2007) Raman optical activity: an incisive probe of molecular chirality and biomolecular structure. *J Mol Struct* 834–836:7–16
110. Acevedo R, Lombardini R, Halas NJ, Johnson BR (2009) Plasmonic enhancement of Raman optical activity in molecules near metal nanoshells. *J Phys Chem A* 113(47):13173–13183
111. Lombardini R, Acevedo R, Halas NJ, Johnson BR (2010) Plasmonic enhancement of Raman optical activity in molecules near metal nanoshells: theoretical comparison of circular polarization methods. *J Phys Chem C* 114(16):7390–7400
112. West JL, Halas NJ (2003) Engineered nanomaterials for biophotonics applications: improving sensing, imaging, and therapeutics. *Annu Rev Biomed Eng* 5(1):285–292
113. Gu FX, Karnik R, Wang AZ, Alexis F, Levy-Nissenbaum E, Hong S, Langer RS, Farokhzad OC (2007) Targeted nanoparticles for cancer therapy. *Nano Today* 2(3):14–21
114. Gobin AM, O’Neal DP, Watkins DM, Halas NJ, Drezek RA, West JL (2005) Near infrared laser-tissue welding using nanoshells as an exogenous absorber. *Lasers Surg Med* 37(2):123–129
115. Jain PK, Lee KS, El-Sayed IH, El-Sayed MA (2006) Calculated absorption and scattering properties of gold nanoparticles of different size, shape, and composition: applications in biological imaging and biomedicine. *J Phys Chem B* 110(14):7238–7248
116. Sun Y, Xia Y (2002) Increased sensitivity of surface plasmon resonance of gold nanoshells compared to that of gold solid colloids in response to environmental changes. *Anal Chem* 74(20):5297–5305
117. Sershen SR, Westcott SL, Halas NJ, West JL (2000) Temperature-sensitive polymer-nanoshell composites for photothermally modulated drug delivery. *J Biomed Mater Res* 51(3):293–298
118. Fiedler VU, Schwarzmaier H, Eickmeyer F, Müller FP, Schoepp C, Verreet PR (2001) Laser-induced interstitial thermotherapy of liver metastases in an interventional 0.5 Tesla MRI system: technique and first clinical experiences. *J Magn Reson Imaging* 13(5):729–737
119. Vogel A, Venugopalan V (2003) Mechanisms of pulsed laser ablation of biological tissues. *Chem Rev* 103(2):577–644
120. Melancon MP, Lu W, Yang Z, Zhang R, Cheng Z, Elliot AM, Stafford J, Olson T, Zhang JZ, Li C (2008) In vitro and in vivo targeting of hollow gold nanoshells directed at epidermal growth factor receptor for photothermal ablation therapy. *Mol Cancer Ther* 7(6):1730–1739
121. Hirsch LR, Stafford RJ, Bankson JA, Sershen SR, Price RE, Hazle JD, Halas NJ, West JL (2002) Targeted photothermal tumor therapy using metal nanoshells. In: *Proceedings of the 24th annual conference and the annual fall meeting of the biomedical engineering society EMBS/BMES conference*, vol 1, Houston, TX, USA, pp 530–531
122. Stern JM, Stanfield J, Kabbani W, Hsieh J-T, Cadeddu JA (2008) Selective prostate cancer thermal ablation with laser activated gold nanoshells. *J Urol* 179(2):748–753
123. O’Neal DP, Hirsch LR, Halas NJ, Payne JD, West JL (2004) Photo-thermal tumor ablation in mice using near infrared-absorbing nanoparticles. *Cancer Lett* 209(2):171–176
124. Shetty A, Elliott AM, Schwartz JA, Wang J, Esparza-Coss E, Klumpp S, Taylor B, Hazle JD, Stafford RJ (2008) Use of gold nanoshells to mediate heating induced perfusion changes in prostate tumors. *Proc of SPIE* 6842:68420S
125. Diagaradjane P, Shetty A, Wang JC, Elliott AM, Schwartz J, Shentu S, Park HC, Deorukhkar A, Stafford RJ, Cho SH, Tunnell JW, Hazle JD, Krishnan S (2008) Modulation of in vivo tumor radiation response via gold nanoshell-mediated vascular-focused hyperthermia: characterizing an integrated antihypoxic and localized vascular disrupting targeting strategy. *Nano Lett* 8(5):1492–1500
126. Diagaradjane P, Shetty A, Wang J, Schwartz J, Park HC, Deorukhkar A, Stafford J, Cho S, Hazle J, Tunnell J, Krishnan S (2008) Modulation of in vivo tumor radiation response via vascular-focused hyperthermia-characterizing gold nanoshells as integrated anti-hypoxic and localized vascular disrupting agents. *Int J Radiat Oncol Biol Phys* 72(1 (Suppl 1)):S64

127. Atkinson RL, Zhang M, Diagaradjane P, Peddibhotla S, Contreras A, Hilsenbeck SG, Woodward WA, Krishnan S, Chang JC, Rosen JM (2010) Thermal enhancement with optically activated gold nanoshells sensitizes breast cancer stem cells to radiation therapy. *Sci Trans Med* 2(55):55ra79
128. Xie H, Diagaradjane P, Deorukhkar AA, Goins B, Bao A, Phillips WT, Wang Z, Schwartz J, Krishnan S (2011) Integrin $\alpha_v\beta_3$ -targeted gold nanoshells augment tumor vasculature-specific imaging and therapy. *Int J Nanomedicine* 6(1):259–269
129. van Vlerken LE, Amiji MM (2006) Multi-functional polymeric nanoparticles for tumour-targeted drug delivery. *Expert Opin Drug Deliv* 3(2):205–216
130. Emerich DF, Thanos CG (2006) The pinpoint promise of nanoparticle-based drug delivery and molecular diagnosis. *Biomol Eng* 23(4):171–184
131. Sershen SR, Westcott SL, West JL, Halas NJ (2001) An opto-mechanical nanoshell-polymer composite. *Appl Phys B Lasers Opt* 73(4):379–381
132. Sershen SR, Halas NJ, West JL (2002) Pulsatile release of insulin via photothermally modulated drug delivery. In: Proceedings of the 24th annual conference and the annual fall meeting of the biomedical engineering society EMBS/BMES conference, vol 1, Houston, TX, USA, pp 490–491
133. Wu G, Mikhailovsky A, Khant HA, Fu C, Chiu W, Zasadzinski JA (2008) Remotely triggered liposome release by near-infrared light absorption via hollow gold nanoshells. *J Am Chem Soc* 130(26):8175–8177
134. Bikram M, Gobin AM, Whitmire RE, West JL (2007) Temperature-sensitive hydrogels with SiO₂-Au nanoshells for controlled drug delivery. *J Control Release* 123(3):219–227
135. Liu H, Chen D, Li L, Liu T, Tan L, Wu X, Tang F (2011) Multifunctional gold nanoshells on silica nanorattles: a platform for the combination of photothermal therapy and chemotherapy with low systemic toxicity. *Angew Chem Int Ed* 50(4):891–895
136. Alivisatos P (2004) The use of nanocrystals in biological detection. *Nat Biotechnol* 22(1):47–52
137. Sun Y, Xia Y (2003) Synthesis of gold nanoshells and their use in sensing applications. In: Unconventional approaches to nanostructures with applications in electronics, photonics, information storage and sensing symposium, vol 776, pp 31–36
138. Tam F, Moran C, Halas N (2004) Geometrical parameters controlling sensitivity of nanoshell plasmon resonances to changes in dielectric environment. *J Phys Chem B* 108(45):17290–17294
139. Wang Y, Qian W, Tan Y, Ding S (2008) A label-free biosensor based on gold nanoshell monolayers for monitoring biomolecular interactions in diluted whole blood. *Biosens Bioelectron* 23(7):1166–1170
140. Hirsch LR, Halas NJ, West JL (2002) A rapid, near infrared, whole blood immunoassay using metal nanoshells. In: Proceedings of the 24th annual conference and the annual fall meeting of the biomedical engineering society EMBS/BMES Conference, vol 2, Houston, TX, USA, pp 1646–1647
141. Hirsch LR, West JL, Jackson JB, Lee A, Halas NJ (2003) A rapid, whole blood immunoassay using metal nanoshells. Proceedings of the 25th annual international conference of the IEEE, vol 4, Cancun, Mexico, pp 3442–3443
142. Khlebtsov B, Dykman L, Bogatyrev V, Zharov V, Khlebtsov N (2006) A solid-phase dot assay using silica/gold nanoshells. *Nanoscale Res Lett* 2(1):6–11
143. Khlebtsov BN, Dykman LA, Bogatyrev VA, Khlebtsov NG (2007) Gold nanoshells as solid-phase dot assay labels. *Proc SPIE* 6534:65343L
144. Khlebtsov B, Khlebtsov N (2008) Enhanced solid-phase immunoassay using gold nanoshells: effect of nanoparticle optical properties. *Nanotechnology* 19(43):435703
145. Ma X, Qian W (2010) Phenolic acid induced growth of gold nanoshells precursor composites and their application in antioxidant capacity assay. *Biosens Bioelectron* 26(3):1049–1055
146. Ma X, Li H, Dong J, Qian W (2011) Determination of hydrogen peroxide scavenging activity of phenolic acids by employing gold nanoshells precursor composites as nanoprobos. *Food Chem* 126(2):698–704

147. Sokolov K, Follen M, Aaron J, Pavlova I, Malpica A, Lotan R, Richards-Kortum R (2003) Real-time vital optical imaging of precancer using anti-epidermal growth factor receptor antibodies conjugated to gold nanoparticles. *Cancer Res* 63(9):1999–2004
148. Zaman RT, Diagaradjane P, Wang JC, Schwartz J, Rajaram N, Gill-Sharp KL, Cho SH, Rylander HG, Payne JD, Krishnan S, Tunnell JW (2007) In vivo detection of gold nanoshells in tumors using diffuse optical spectroscopy. *IEEE J Select Topics Quantum Electron* 13(6):1715–1720
149. Zaman RT, Diagaradjane P, Wang JC, Schwartz J, Rajaram N, Gill-Sharp KL, Cho SH, Rylander HG III, Payne JD, Krishnan S, Tunnell JW (2008) Erratum to In vivo detection of gold nanoshells in tumors using diffuse optical spectroscopy. *IEEE J Select Topics Quantum Electron* 14(1):251–251
150. Kah JCY, Chow TH, Ng BK, Razul SG, Olivo M, Sheppard CJR (2009) Concentration dependence of gold nanoshells on the enhancement of optical coherence tomography images: a quantitative study. *Appl Opt* 48(10):D96–D108
151. Kah JCY, Olivo M, Chow TH, Song KS, Koh KZY, Mhaisalkar S, Sheppard CJR (2009) Control of optical contrast using gold nanoshells for optical coherence tomography imaging of mouse xenograft tumor model in vivo. *J Biomed Opt* 14(5):054015
152. Park J, Estrada A, Sharp K, Sang K, Schwartz JA, Smith DK, Coleman C, Payne JD, Korgel BA, Dunn AK, Tunnell JW (2008) Two-photon-induced photoluminescence imaging of tumors using near-infrared excited gold nanoshells. *Opt Express* 16(3):1590–1599
153. Park J, Estrada A, Schwartz JA, Payne JD, Dunn AK, Tunnell JW (2008) 3D microscopy of gold nanoshells in tumors using two-photon-induced photoluminescence. *Proc SPIE* 6869:68690L
154. Park J, Estrada A, Sharp K, Sang K, Schwartz JA, Smith DK, Coleman C, Donald PJ, Korgel BA, Dunn AK, Tunnell JW (2008) Two-photon-induced photoluminescence imaging of tumors using near-infrared excited gold nanoshells. In: Conference on lasers and electro-optics and conference on quantum electronics and laser science, vol 1, pp 1–2
155. Park J, Estrada AP, Diagaradjane K, Sharp K, Sang J, Schwartz A, Coleman C, Payne JD, Dunn AK, Krishnan S, Tunnell JW (2008) Microscopy of gold nanoshells in tumors using two-photon induced photoluminescence, Digest of the IEEE/LEOS Summer Topical Meetings, 1:71–72
156. Puvanakrishnan P, Park J, Diagaradjane P, Schwartz JA, Coleman CL, Gill-Sharp KL, Sang KL, Payne JD, Krishnan S, Tunnell JW (2009) Narrow band imaging of tumors using gold nanoshells. *Proceedings of SPIE* 7169:716912
157. Puvanakrishnan P, Park J, Diagaradjane P, Schwartz JA, Coleman CL, Gill-Sharp KL, Sang KL, Payne JD, Krishnan S, Tunnell JW (2009) Near-infrared narrow-band imaging of gold/silica nanoshells in tumors. *J Biomed Opt* 14(2):024044
158. Xie H, Wang ZJ, Bao A, Goins B, Phillips WT (2010) In vivo PET imaging and biodistribution of radiolabeled gold nanoshells in rats with tumor xenografts. *Int J Pharm* 395(1–2):324–330
159. Garrett N, Whiteman M, Moger J (2011) Imaging the uptake of gold nanoshells in live cells using plasmon resonance enhanced four wave mixing microscopy. *Opt Express* 19(18):17563–17574
160. Zhan P, Liu JB, Dong W, Dong H, Chen Z, Wang ZL, Zhang Y, Zhu SN, Ming NB (2005) Reflectivity behavior of two-dimensional ordered array of metallodielectric composite particles at large incidence angles. *Appl Phys Lett* 86(5):051108
161. Graf C, van Blaaderen A (2002) Metallodielectric colloidal core-shell particles for photonic applications. *Langmuir* 18(2):524–534
162. Tserkezis C, Gantzounis G, Stefanou N (2008) Collective plasmonic modes in ordered assemblies of metallic nanoshells. *J Phys Condens Matter* 20(7):075232
163. Stefanou N, Tserkezis C, Gantzounis G (2008) Plasmonic excitations in ordered assemblies of metallic nanoshells. *Proceedings of SPIE* 6989:698910

164. Fano U (1961) Effects of configuration interaction on intensities and phase shifts. *Phys Rev* 124(6):1866–1878
165. Bachelier G, Russier-Antoine I, Benichou E, Jonin C, Del Fatti N, Vallée F, Brevet P-F (2008) Fano profiles induced by near-field coupling in heterogeneous dimers of Gold and Silver nanoparticles. *Phys Rev Lett* 101(19):197401
166. Boller K-J, Imamolu A, Harris SE (1991) Observation of electromagnetically induced transparency. *Phys Rev Lett* 66(20):2593
167. Fleischhauer M, Imamoglu A, Marangos JP (2005) Electromagnetically induced transparency: optics in coherent media. *Rev Mod Phys* 77(2):633
168. Mirin NA, Bao K, Nordlander P (2009) Fano resonances in plasmonic nanoparticle aggregates. *J Phys Chem A* 113(16):4028–4034
169. Lassiter JB, Sobhani H, Fan JA, Kundu J, Capasso F, Nordlander P, Halas NJ (2010) Fano resonances in plasmonic nanoclusters: geometrical and chemical tunability. *Nano Lett* 10(8):3184–3189
170. Fan JA, Wu C, Bao K, Bao J, Bardhan R, Halas NJ, Manoharan VN, Nordlander P, Shvets G, Capasso F (2010) Self-assembled plasmonic nanoparticle clusters. *Science* 328(5982):1135–1138
171. Liu N, Weiss T, Mesch M, Langguth L, Eigenthaler U, Hirscher M, Sönnichsen C, Giessen H (2010) Planar metamaterial analogue of electromagnetically induced transparency for plasmonic sensing. *Nano Lett* 10(4):1103–1107
172. Verellen N, Sonnefraud Y, Sobhani H, Hao F, Moshchalkov VV, Dorpe PV, Nordlander P, Maier SA (2009) Fano resonances in individual coherent plasmonic nanocavities. *Nano Lett* 9(4):1663–1667
173. Peña-Rodríguez O, Pal U, Campoy-Quiles M, Rodríguez-Fernández L, Garriga M, Alonso MI (2011) Enhanced Fano resonance in asymmetrical Au:Ag heterodimers. *J Phys Chem C* 115(14):6410–6414
174. Halas NJ, Lal S, Chang W-S, Link S, Nordlander P (2011) Plasmons in strongly coupled metallic nanostructures. *Chem Rev* 111(6):3913–3961